JGR Planets

RESEARCH ARTICLE
10.1029/2024JE008915

Key Points:

- We study the water flows surrounding Tooting crater in Amazonis Planitia due to a recent impact
- Dramatic erosion by hot water determined channel incisions, waterfalls, and lakes now observed as large pits
- Caverns were formed along long fractures probably due to the impact, and slope lineae along pit slopes were re-activated by the heat wave

Supporting Information:

Supporting Information may be found in the online version of this article.

Correspondence to:

F. V. De Blasio,
fabio.deblasio@unimib.it

Citation:

De Blasio, F. V., Caccia, A., & Crosta, G. B. (2025). Transient hydrology in Amazonis Planitia (Mars) in the aftermath of the tooting impact. *Journal of Geophysical Research: Planets*, *130*, e2024JE008915. https://doi.org/10.1029/2024JE008915

Received 29 JAN 2025
Accepted 28 OCT 2025

Author Contributions:

Conceptualization: Fabio Vittorio De Blasio
Data curation: Fabio Vittorio De Blasio, Andrea Caccia
Formal analysis: Fabio Vittorio De Blasio, Andrea Caccia
Investigation: Fabio Vittorio De Blasio, Andrea Caccia, Giovanni Battista Crosta
Methodology: Fabio Vittorio De Blasio, Andrea Caccia, Giovanni Battista Crosta
Supervision: Fabio Vittorio De Blasio
Validation: Andrea Caccia, Giovanni Battista Crosta
Visualization: Fabio Vittorio De Blasio, Andrea Caccia, Giovanni Battista Crosta
Writing – original draft: Fabio Vittorio De Blasio

Transient Hydrology in Amazonis Planitia (Mars) in the Aftermath of the Tooting Impact

Fabio Vittorio De Blasio[1], Andrea Caccia[1], and Giovanni Battista Crosta[1]

[1]Department of Earth and Environmental Sciences, University of Milano Bicocca, Milan, Italy

Abstract Hydrological flows generated by meteoroid impact are still largely unexplored on Mars and may also have implications for Earth. We reconstructed the hydrological sequence initiated on Mars by a less than 3 Ma old meteoroid impact that formed the 28 km-wide Tooting crater on Amazonis Planitia, an ice-bearing region. Significant thermal and mechanical erosion were produced by the temporary rivers created by the impact on the icy terrain. Through analysis of CTX and HiRISE imagery supplemented with hydrological calculations, we inferred that the meltwater flowed approximately 80 km, eroding deeply the soil. Upon encountering an extensive (more than 100 km) impact-induced fracture line network, the water plummeted in vertical waterfalls, creating thermokarst caverns and ephemeral lakes. Secondary water springs are hypothesized to stem from the impact of ballistic ejecta blocks. Our analysis reveals that the initial hydrologic activity took a short time (hours to one day), while thermal effects were more durable but still geologically rapid. HiRISE imagery reveals slope streaks inside the emptied lacustrine basins. Lines, which emerge from a deep regolith layer, are potentially indicative of aquifer-fed water springs. The consistent origination of multiple lineae at the same stratigraphic level hints at significant subsurface re-mobilized water or ice, when heat was released from temporary warm lakes.

Plain Language Summary About 3 million years ago, an asteroid struck an ice-bearing terrain in Amazonia Planitia near Olympus Mons on Mars, an area which has been hypothesized to be the floor of an ancient Martian ocean. In this study, we found that the impact, which formed a crater approximately 30 km wide named Tooting, generated a significant amount of meltwater, giving rise to temporary rivers both from the ejecta and from distant areas. This meltwater encountered a broad fracture line, likely created by the impact itself, giving rise to impressive waterfalls and underground caverns. This mass of water eventually filled three lakes through processes that unfolded rapidly in geological terms but left lasting traces. Today, these former lakes are evident as wide pits with numerous slope streaks visible on their sides. These astrobiologically interesting streaks could originate from water flow, particularly from springs at the tops of the pits, where layers of brine melted due to the heat of the transient lakes and from the sun.

1. Introduction

Large asteroid impacts on Mars represent a probe of the nature of the Martian soil, in particular regarding the possible presence of subsurface ice. Significant research has focused on understanding the morphology of ejecta resulting from old impacts on icy terrain, as documented by Barlow and Perez (2003), Barlow et al. (2005) and Senft and Stewart (2008). Recent findings by Dundas et al. (2023) highlight a small (150 m) crater recently formed at a relatively low (35°) latitude that reveals sub-surface ice in its ejecta. In some particular cases, extensive amounts of water are released during impact events (Wang et al., 2005), with consequent carving of particular channel-shaped morphologies (Harrison et al., 2010). Such morphologies, though not entirely caused by impact events, are evident in Figure 1, which shows extensive fossil river networks in Hephaestus Fossae, west of Elysium Mons, deeply carved into the Martian soil (Rodriguez et al., 2012).

Apparently, water was involved in carving the terrain, and gave origin at some locations to cavities (Figure 1a), which were now transformed to talus pits due to subsequent rockfall activity (Figures 2b and 2c). These features are normally attributed to thermokarst. In such scenario, detailed in Figure 1d, the melting of ground ice leads to subsidence and the formation of karst-like topographic features (Washburn, 1980). This can occur due to direct climate warming, volcanic and plutonic processes, active layer slope erosion, slumping, soil creep, deflation, or lateral degradation from warm surface water seepage. The generated topographic depressions include thaw lakes, alases, and thermokarst mounds (French, 2007), which are distinguished by their shapes, sizes, and the context of

Writing – review & editing: Fabio Vittorio De Blasio, Giovanni Battista Crosta

their formation and can all be found both on Mars and on Earth (Costard & Kargel, 1995; De Blasio et al., 2024; Soare et al., 2008). These features are typically absent in bedrock areas. Surface disturbance and the melting of ground ice lead to water impoundment, or thermokarst lakes, and positive feedback loops that accelerate permafrost thaw. On Mars, thermokarst features have been identified as irregularly shaped depressions, particularly in outflow channels and plains (Costard & Baker, 2001; Costard & Kargel, 1995; Dundas et al., 2015; Morgenstern et al., 2007), suggesting a similar process of thermal erosion, possibly induced by warm floods, analogous to terrestrial outflow channels during snowmelt (Costard et al., 1999).

The role of magmatic activity and possibly mud volcanism in shaping the landscape like the one in Hephaestus Fossae is also considered as a possible interpretation (Dapremont & Wray, 2021; Nerozzi et al., 2020; Rodriguez et al., 2012). Notably, at least two large impact craters, situated amidst these river networks (indicated by red arrows in Figure 1a and detailed in Figure 1d), raise questions about their involvement in generating water for the superficial drainage system. These images show that water released from the cryosphere by the impact was likely involved in shaping the ground fractures that were present in the region. The characteristic flow-like ejecta patterns on Mars, including double and multiple-layered types, also suggest the participation of ice in the morphology resulting from impacts (Barlow et al., 2005). This leads to speculation as to whether these craters contributed to the availability of water for the river networks. Furthermore, calculations show that the impact of large asteroids on Mars can release a large amount of energy, producing temporary hydrothermal systems (Rathbun & Squyres, 2002). Additional evidence of fluvial channels carved by water flows, possibly resulting from impacts on ice-rich terrain, further supports this hypothesis (Baker et al., 2015; Rathbun & Squyres, 2002). Notice that the complex landforms of Hephaestus Fossae (Figure 1a) probably result from different processes involving the cryosphere and volcanic processes. However, the northern crater in Figure 1d has a series of features that are here attributed to the effect of an impact on the icy surface. These features include the presence of channels clearly due to the water flow from the crater outward (and the fact that flow direction is consistent with terrain gradient), and teardrop-shaped islands indicating the flow direction of water. These water flows were created (or were affected) by caverns in the deep soil, probably resulting from either previous volcanic activity from Elysium Mons or by the heat content of water that seeped from the impact through the terrains.

This paper provides additional evidence supporting the existence of a transient hydrothermal system on Mars triggered by the release of water from a documented asteroid impact. The Hephaestus Fossae event is shown in Figure 1 is complex due to the vast area it covers and the presence of volcanic and potentially hypoabyssal activities, which may have contributed to the melting of the hydrosphere (Rodriguez et al., 2012). Therefore, we focus on the better interpretable morphologies related to the Tooting crater (Mouginis-Mark & Boyce, 2012), a prominent feature of the area called Amazonis Planitia (Figure 2). Some evidence for the presence of abundant sub-surface ice in this area is both morphological and geophysical. Morphology includes alleged rootless cones formed by vapor heated by lavas from Elysium Mons (Lanagan et al., 2001) and polygonal patterned terrains (Lucchitta et al., 1986). Geophysical probes such as radar measurements (Campbell et al., 2008), and dielectric property (Mouginot et al., 2012; Jankowski & Squyres, 1993) also indicate abundant ice in the form of ice-rich regolith (Murray et al., 2006; Page, 2007). Moreover, this area has been posited to be part of the southernmost basin of the hypothetical ancient Martian ocean that may have filled the northern plains known as Vastitas Borealis (Baker et al., 1991; Carr, 2006; Carr & Head, 2003; De Blasio, 2018; Dickeson & Davis, 2020; Head et al., 1999; Parker, 1994; Parker et al., 2010). Whether this ice derives from the freezing of the ancient ocean (Clifford & Parker, 2001) or has a different origin, such as a scenario alternating lava flows with dewatering from the Olympus Mons aureole and flooding from Marte Valles (Fuller & Head, 2002), is, however, not central for the present work.

The Tooting impact offers several further advantages for study: (a) the morphologies associated with the water released upon impact are visible, and high-quality imagery is available; (b) the areas surrounding the crater for several hundred kilometers around all sides except east are extremely smooth and flat; (c) the crater considerable size implies a large impactor and substantial energy release; (d) the recent nature of the impact (Mouginis-Mark & Boyce, 2012) ensures the well preserved state of the associated morphologies; (e) the impact occurred on an ice-rich terrain. Note that the presence of extensive ground ice in Amazonis Planitia (AP), where Tooting is located, and more broadly in the northern lowlands, is still a subject of debate. Based on geophysics (Garvin et al., 2024), some studies argue that dielectric property analysis based on radio wave reflectors does not conclusively indicate the presence of ice (Campbell et al., 2008). In contrast, other research points to the existence of thick (decameters)

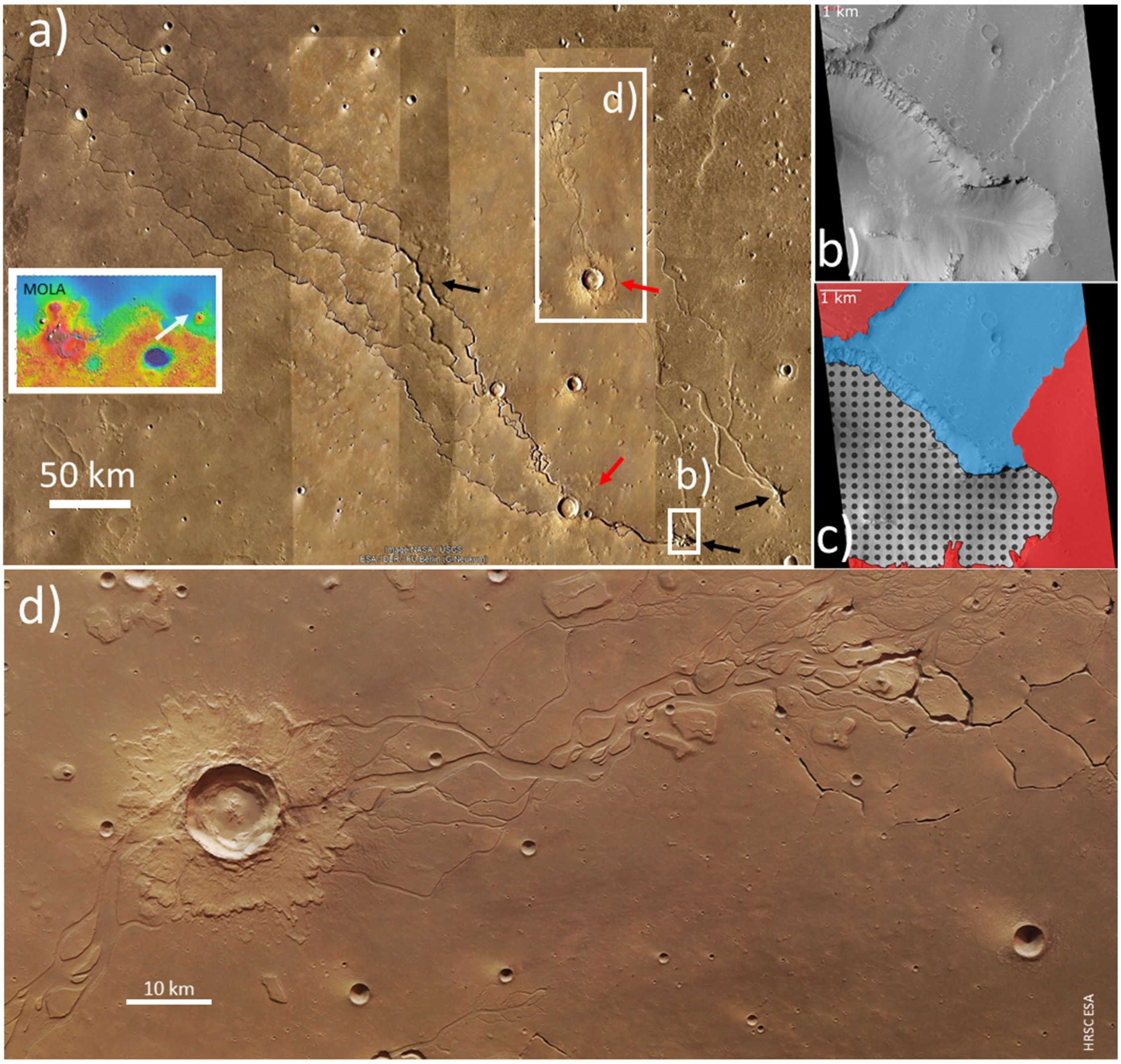

Figure 1. Hephaestus Fossae is a prominent example of deep water erosion produced by meteoroid impact at the surface of Mars. (a) CTX image of the area showing numerous watercourses carved by water. The craters from which ice was melted are indicated with red arrows. Black arrows show the position of some of the caverns and pits scoured by hot water springing from the impact areas. One of the pits is shown in detail in panel (b), and the interpreted image is shown in panel (c). Red: soil untouched by water. Blue: channel. The pit is the dotted area. The position of Hephaestus Fossae on Mars is shown in the inset in panel (a). (d): magnified area in panel (a) (white rectangle, with north pointing to the right and some topographic elevations indicated).

ice layers in the nearby Arcadia Planitia just north of AP (Bramson et al., 2015). Thus, the aim of our work is to contribute to this discussion through a detailed morphological analysis.

The Tooting impact is thus examined as a "probe" of the ground material down to a depth of at least 2 km, with the main goal of describing the sequence of hydrological events based on the hypothesized presence of abundant ground ice in the impact zone. We begin by examining selected properties of the crater relevant to the hydrology. Subsequently, we identify the hydrological springs: a primary source within the crater vicinity and secondary water springs located further afield. Our analysis then shifts to the erosion patterns caused by the water torrents generated upon impact, including the three erosion basins that possibly hosted the ephemeral lakes and were shaped by them. We estimate the timeline for this hydrological cycle development and the cooling duration for the heated water. Further, we explore the slope streaks inside these pits, which may indicate an aquifer reactivated by the thermal energy delivered by the warm water within the AP ground material. This study is supplemented with two Appendices detailing the data sources and methods, further data on the Tooting crater and the slope streaks, and the mathematical details of our analytical model for the calculation of the flow length of slope streaks on a talus within the pits.

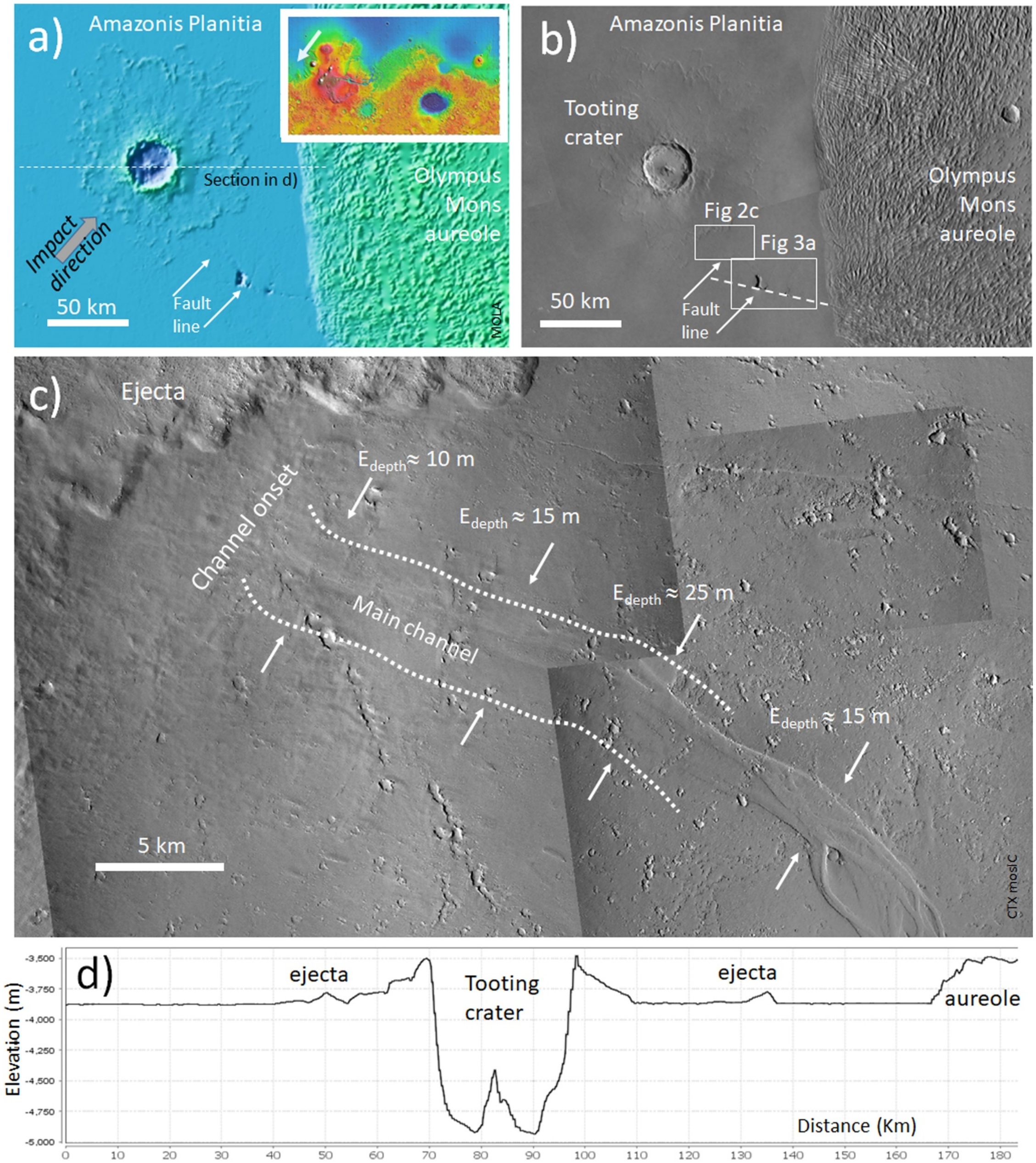

Figure 2. General view of Tooting crater and of the erosive water flow and its products. (a) crater Tooting shown on a MOLA colorized map; the position of Tooting in the global Mars is shown in the inset. The image of the area shows Tooting incised on Amazonis Planitia and the aureole to the east, a feature from the Olympus Mons volcano. Arrows point to the water channel created by the impact. (b) the corresponding area shown in an optical image (CTX mosaic). (c) detailed image of the area highlighted in panel (b) showing the ejecta and the erosional features created by the temporary torrents ("main channel") at the boundary between the ejecta and the plains. To drive the eye, the initial 20 km of channel are highlighted with dotted lines. (d) MOLA elevation through the section shown in panel (a).

2. Methods and Data

The images analyzed in this work are derived from the optical Context Camera CTX aboard the Mars Reconnaissance Orbiter (Malin et al., 2007) and the infrared THEMIS images (Thermal Emission Imaging System) onboard the Mars Odyssey mission (Christensen et al., 2004). We also utilized high-resolution images from HRSC (High-Resolution Stereo Camera) aboard Mars Express (Neukum & Jaumann, 2004) and HiRISE (High Resolution Imaging Science Experiment) aboard the Mars Reconnaissance Orbiter. Altimetry data based on the JMARS platform (Java Mission-planning and Analysis for Remote Sensing), provided and updated by Arizona State University, incorporated information from the Mars Orbiter Laser Altimeter (MOLA) aboard the Mars

Global Surveyor mission (MGS, Smith et al., 2001). MOLA provided satisfactory resolution for detailed features spanning more than a few kilometers.

3. Observations

3.1. The Tooting Crater

The Tooting crater (Mouginis-Mark & Boyce, 2012; 23°10′N and 152°12′W) was excavated on the largely level terrain of AP (Figure 2). Apart from the Olympus Mons aureole, no significant topographical features can be observed in the vicinity before the impact. The crater spans an average diameter of 28 km and lies at an elevation of about −3,870 m, according to MOLA data (Figure 2). Positioned on a smooth, horizontal surface that was resurfaced approximately 240–375 million years ago (Mouginis-Mark & Boyce, 2012), the crater's geometry and ejecta thickness can be quite accurately determined by subtracting the average elevation of the surrounding area from individual MOLA readings (Mouginis-Mark & Boyce, 2012; Mouginis-Mark & Garbeil, 2007; Sturm et al., 2016). The resulting volume of the crater cavity is 380 km^3, while the volume of material above the −3,872 m elevation is approximately 425 km^3 (Mouginis-Mark & Garbeil, 2007). The discrepancy between these figures may be due to uncertainties in the estimates, by partial filling due to Martian dust after the excavation of the crater, by the bulking resulting from rock fragmentation, and by the transformation of ice into water as documented in this study. Tooting crater represents an exemplary model of multiple-layered ejecta (MLE) impact craters (Barlow et al., 2005). In an impact on an ice-laden surface, the uppermost material is ejected at high speed and undergoes significant evaporation. The vapourized material forms a vapor plume that expands during the final stages of crater development, not interacting with the materials expelled earlier (Weiss & Head, 2013, 2014). The central peak within the Tooting crater stands approximately 1,000 m above the crater bottom (Mouginis-Mark & Garbeil, 2007). Ejecta around Tooting exhibit varying thicknesses, with the thickest layers near the crater, suggesting a multi-stage ejection process. Typically, MLE craters display radial symmetry in their ejecta distribution, indicative of a singular outward-sliding emission of material. However, Tooting's ejecta pattern deviates from this norm, displaying a slight asymmetry—a detail apparent in the MOLA data (Figure 2a). This irregularity is theorized to stem from the asteroid's shallow angle of impact, as the adjacent topography shows no gradient that might otherwise direct the ejecta's flow trajectory (Figure 1; Mouginis-Mark & Garbeil, 2007). By assuming a level pre-impact surface and referencing the surrounding terrain's elevation at −3,872 m from MOLA data, it is possible to analyze the spatial distribution in Tooting's ejecta layer thickness (Mouginis-Mark & Boyce, 2012; Sturm et al., 2016). Notably, to the south of the crater, the ejecta are remarkably thin, measuring a mere 3–5 m deep even at a distance of roughly 11 km from the crater's rim. This observation contributes to our understanding of the impact dynamics and the subsequent distribution of ejected materials.

Remarkably, Tooting is relatively young for its size, with an estimated age of about 2.9 million years (Mouginis-Mark & Boyce, 2012). A cross-section of the crater (Figure 2d) reveals that its southernmost point reaches a depth of approximately −5,000 m (−4,900 m in this section). The surrounding terrain, which represents the pre-impact level, maintains a consistent elevation of about −3,870 m below the datum, with minimal variation over an expanse of 10,000 km^2 (Figure 2d).

3.2. The Primary Water Source

Water carved out three primary channels: a "main channel" stemming from the impact area and extending from NW to SE (Figures 2c, 3a, 3b), and two less incised N-S "secondary" channels (Figure 3a). Apparently, these incised channels appear similar to river channels on Earth resulting from mechanical erosion by water. Note the levees, the slightly meandering pattern, and the presence of teardrop-shaped islands within the channels (Figures 3a–3c). The depth of erosion reached up to 15 m, which can be compared to terrestrial rivers in their middle course (Huggett & Shuttleworth, 2022). However, on Earth, such erosion depths are reached in time spans of 1,000–10,000 years corresponding to erosion rates of 0.02 mm/a or less (Schaller et al., 2001). Data presented in this paper indicate that the timing of the channel incision was much shorter (Section 4), which requires a comparably faster erosion rate. Due to the expected high temperature of water after release from the impact area, it can be suggested that channels were incised not only mechanically but also thermally, which would explain the deep incisions attained in a relatively short time (see further discussion on timing of the events). The main channel stretches for 30–60 km in length and is 10–15 m deep, paralleling the south eastern ejecta flow (Figure 2c), although its origin remains ambiguous. Given that large craters often contain water from the impact zone

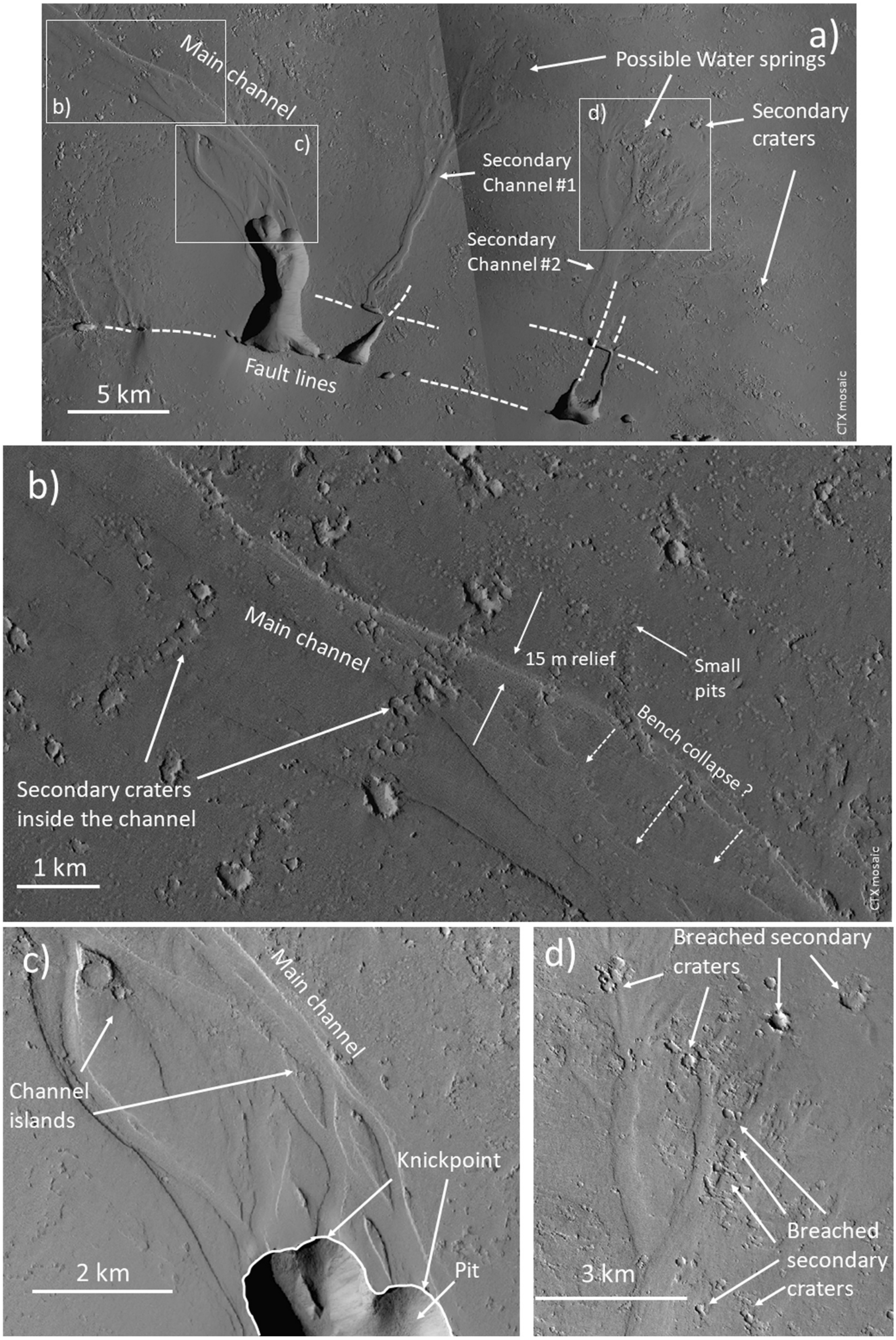

Figure 3. Details of the terminal area where water was captured by the fault line and pounded temporarily. (a) general view (white square in Figure 2b shows the location). (b) the channel area (see 3a for reference). (c) Islands formed in the channels in proximity of the pits. (d) detail of the secondary springs and breached secondary craters. All images were taken with CTX on board the Mars Reconnaissance Orbiter.

(Rathbun & Squyres, 2002), it is plausible that warm water accumulated within the Tooting crater. However, the absence of breaches along the crater rim suggests that the primary water source did not originate from within the crater and was possibly caused by the stress (mechanical and thermal) following the impact. The water could have been released by the emplacement of the ejecta onto an ice-covered surface, a mechanism similar to the one suggested for the much larger (220 km) Lyot crater (Harrison et al., 2010; Weiss et al., 2017).

3.3. Secondary Springs

The diverse orientation of the channels depicted in Figure 3a suggests the existence of multiple independent water springs. The secondary channels materialize from indistinct secondary water springs located in regions not impacted by the ejecta (Figures 3a and 3d). The direction of the slope gradient indicates the southward movement of the water. The absence of any major morphology indicating an origin for these secondary streams makes the source difficult to pinpoint. Further in the paper, we will provide additional information on these water sources.

3.4. Secondary Craters

The landscape is dotted with numerous secondary craters, and Figures 3b and 3d show only a sketch of the most prominent ones. These craters are visible across the flat and smooth areas of AP (see Figures 3a, 3b, and 3d), and in Figure 3d, it is possible to appreciate the traces of breaching near the sources of the two secondary streams. As shown in Figure 3b, secondary craters are found inside the channels. Because secondary impactors are flung at high speed during the impact stage and the impacts craters found within the channels show evident signs of water-related erosion, these craters necessarily precede the water flow. Thus, they must have been exposed to flowing water, which indicates that the craters were deeper than the 15 m of the surface erosion (Figure 3b).

3.5. The Channels

Figure 3 shows the details of the channels that conveyed southward the water from both primary and secondary sources. Similar to Earth, some teardrop-like islands eroded by the flow are present inside the channels (Figure 3c), allowing us to infer that the flow was directed southward (note the crater at the front of the island in Figure 3c protecting the rest of the island from erosion). The erosion marks from the primary source deepen eastward, from about 10 m near the ejecta to about 15–25 m some tens of kilometers downstream. These flows exhibit a dendritic pattern at their source, similar to river systems on Earth, branching southward before converging into two distinct channels ("Channel 1" and "Channel 2" in Figure 3). Although the poorly developed branches and limited erosion suggest a short-lasting process, the erosion from the secondary sources indicates that water originated from them and flowed southward.

3.6. The Pits

The water produced by the melting of ground ice was likely channeled into the fracture lines, forming six main possible thermokarst cavities, or "pits," and some minor ones deep into the fractures. The steep heart-shaped scarp at the boundary between the river and the pit and the abrupt erosion of the tear-drop islands on the surface of the channel suggest that the water initially cascaded into these pits, retrogressively deepening the step from the main channel to the pit, which resulted in a morphology similar to a waterfall. The knickpoint of the fossil waterfall of the largest pit is indicated in Figure 3c. Pits are about 2–3 km wide (meant here as the distance parallel to the fractures), 1 km deep (measured through a MOLA section with orbital shots cutting through the western pit), and of different lengths. Based on MOLA data, we measured the length, area, and volume of the longest pit. They are, respectively, about 8 km, 20 km^2, and 13 km^3 (after subtraction of the talus volume). Considering that the average width is 2.7 km, it can be suggested that the process of waterfall erosion was retrogressive in a thermally erodible soil.

4. Analysis of the Hydrological History and Discussion

4.1. Water Produced at Impact

In this section, observations will be interpreted in terms of water produced by the Tooting impact. Based on the present width of the crater (28 km), and considering that craters on Mars are approximately one-tenth the size of the impactor (e.g., Barlow & Bradley, 1990 and references therein), it follows that the impactor that created

Tooting had an approximate radius of 1.4 km. Its mass $M \approx \frac{4}{3}\pi R^3 \rho$ is estimated at $\approx 4.4 \times 10^{13}$ Kg for a meteorite of average density (ρ) of $4,000 \, \frac{\mathrm{Kg}}{\mathrm{m}^3}$ (Flinn et al., 2018; Ostrowski & Bryson, 2019). The kinetic energy was so $\mathrm{K} = \frac{1}{2}\mathrm{MU}^{2\cdot}$ or $K \approx 2 \times 10^{21}$–$10^{22}$J depending on the impact velocity of the asteroid (here velocities of 10 and 30 km/s are used as extremal values). Slightly lower or higher energies would be obtained using chondritic and metallic compositions, respectively, and it is clear that there is an ample uncertainty in this estimate.

If this energy were fully converted to melting ice, it could theoretically produce a mass $M_{\mathrm{melt}} \approx \frac{K}{C\Delta T + \lambda}$Kg of meltwater (where C, λ are the specific heat and latent hear for ice melting), and using $K \approx 2 \times 10^{21}$J, $\Delta T \approx 100$ K, it follows a mass of $M_{\mathrm{melt}} \approx 4 \times 10^{15}$ Kg corresponding to ice volume of more than 4,000 km^3. For comparison, it was estimated by Horvath and Andrews-Hanna. (2024) that the Jezero Crater had a surface runoff of $\approx$2 Km^3/yr during its period of hydrological activity. The amount of meltwater estimated here is exaggerated, partly because only a small portion of the impact energy is transformed into heat (Melosh, 1989), and only part of this share goes into ice melting. Moreover, ice in the Martian soil occupies a fraction of the porous ground volume (Clifford & Hillel, 1983). Despite these uncertainties, it is clear that the impact energy was sufficient to melt a considerable volume of ice. Consequently, the quantity of water produced was constrained by the available subsurface ice rather than the energy of the impact.

4.2. Water Produced at the Secondary Springs

4.2.1. Heat Diffusion

The mechanism behind the water release from the secondary sources is unclear. One possible hypothesis is that the heat generated by the main impact diffused through the soil to a certain depth, melting subsurface ice upon reaching the areas where the secondary springs are now observed.

The time τ required for a heat wave to diffuse to a certain distance δ is very approximately

$$\delta \approx \left(\frac{\chi}{\rho C}\tau\right)^{\frac{1}{2}} \tag{1}$$

where $\chi \approx 1 - 3 \, \frac{W}{\mathrm{m}^2}$ is the thermal conductivity of rock, $C \left(\frac{\mathrm{J}}{\mathrm{Kg\ K}}\right)$ is the heat capacity, and $\rho \, \left(\frac{\mathrm{Kg}}{\mathrm{m}^3}\right)$ is the density (see data in Table 1). Expressing the diffusion distance δ_m in meters and τ_c in centuries, the constant $\frac{\chi}{\rho C}$ yields $\delta_m \approx 55 \, \sqrt{\tau_c}$, or equivalently $\tau_c \approx 3.3 \times 10^{-4} \, \delta_m^2$. Thus, if heat diffusion is the most efficient heat transfer process, it would take approximately 1 million years for the heat from the impact to travel over distances of tens of kilometers where the secondary springs are located. This implies a significantly delayed water release from the secondary springs long after the main impact event. While a faster mechanism, such as water being driven through fractures by a hydrothermal system, could be at work (Newsom, 2010), the diffusion coefficient would need to be unrealistically high—around 10^6 times greater than that of bare rock—to reduce the timeframe to about a thousand years. Numerical calculations for the thermal history of the areas surrounding heated lakes indicate that with realistic permeabilities for Martian soil, the diffusion time for heat to distances of one—two crater diameters is between a hundred thousand years and several million years (Abramov & Kring, 2005; Newsom, 2010; Rathbun & Squyres, 2002). In particular, Abramov and Kring (2005) studied the post-impact diffusion of heat from a crater of the size of Tooting and found results in line with our estimates with a shorter time span. One problem with this hypothesis is that the heat diffuses to larger volumes from the heated impact area, and the temperature would drop approximately as $T \propto T_0 \left(\frac{R_0}{R}\right)^3$ from an initial value T_0 from a radius R_0 to a larger one R. Using $T_0 \approx 150$ °C = 423 K, $R_0 \approx 7$ Km for the simulation of a 30-km wide crater 25 years after the impact (Newsom, 2010), it follows that only a few degrees of excess temperature would remain after R of some tens of km. Thus, heat generated by the main impact as a source of secondary springs does not seem a viable suggestion.

4.2.2. Energy of Secondary Impactors

A possible alternative hypothesis is that the energy from the ice melt in the secondary springs was provided by the impact of secondary meteoroids from the Tooting impact. We thus evaluate the velocity of secondary impactors from the area of the main impact

Table 1
Physical Parameters, Their Units, and Numerical Values Assumed for the Ice-Rock Mixture

Quantity	Latent heat λ	Specific heat, ice C_I	Specific heat, rock C_R	Temperature difference ΔT	Ice, density ρ_I	Rock, density ρ_R
Units	$\frac{\mathrm{J}}{\mathrm{kg}}$	$\frac{\mathrm{J}}{\mathrm{Kg\ K}}$	$\frac{\mathrm{J}}{\mathrm{Kg\ K}}$	°C	$\frac{\mathrm{Kg}}{\mathrm{m}^3}$	$\frac{\mathrm{kg}}{\mathrm{m}^3}$
Numerical value	3.3×10^5	1,880	1,230	150°	920	2,700

$$v = \left(\frac{g\,r}{\sin(2\theta)}\right)^{\frac{1}{2}} \tag{2}$$

and find velocities of at least $v \approx 500$ m/s to 1,000 m/s in order to reach the observed distances of about 70 km if launched at an angle $\theta = 45°$. Assuming that the secondary impact craters of diameter of some hundred meters were produced by blocks of diameter $\phi \approx 50$–100 m and using a density $\rho = 3{,}000\,\frac{\mathrm{kg}}{\mathrm{m}^3}$ for the density, we find masses for the secondary blocks of about

$$m = \frac{4}{3}\pi\left(\frac{\phi}{2}\right)^3 \rho \approx 1.87 \times 10^8 \text{ kg and } 1.5 \times 10^9 \text{ kg}, \tag{3}$$

and kinetic energy

$$E_k \approx 2.42 \times 10^{13}\,J - 10^{15}\,J \tag{4}$$

4.2.3. Ice Melted at Impact?

If the kinetic energy in Equation 4 were transformed into heat with efficiency e, the volume of water produced would be

$$V_w = e\,\frac{E_k}{\left(\rho_I C_I \epsilon + \rho_R C_R (1-\epsilon)\right)\Delta T + \rho_I \epsilon \lambda} = \frac{e}{2}\,\frac{V_{\mathrm{imp}}\rho_{\mathrm{imp}} u^2}{\left(\rho_I C_I \epsilon + \rho_R C_R (1-\epsilon)\right)\Delta T + \rho_I \epsilon \lambda} \tag{5}$$

where we assume a volumetric percentage of ice ϵ in the soil and where λ, C_I, C_R are respectively the latent heat, the specific heat of ice and that of rock, ρ_I, ρ_R the densities of ice and rock, V is the bulk volume of ice-bearing rock that has reached at least 100°C of temperature, ΔT is the difference between the melting temperature and the initial soil temperature, and V_{imp} is the volume of the impactor. We refer to Section 4.4.2 for a discussion of the values of these parameters. Here, we estimate that water volumes between 10^4 em^3 and 5×10^4 em^3 would be produced by one secondary impact on pure ice, $\frac{V_w}{V_{\mathrm{imp}}} \approx e\,\frac{u^2}{4\times10^5}\,\frac{\rho_{\mathrm{imp}}}{\rho_I}$. These estimates are consistent with the numerical impact calculations by Pierazzo et al. (1997) and Barr and Citron (2011) indicating that ice-on-ice impacts would produce a water volume a few 10 times larger than the impactor volume at a speed of $5\,\frac{\mathrm{km}}{\mathrm{s}}$. However, as shown earlier, secondary impact velocities are considerably lower, and based on Barr and Citron (2011), much smaller water volumes on the order of the impactor volume would be produced at secondary impact velocities of $0.5 - 1\,\frac{\mathrm{km}}{\mathrm{s}}$, assuming $e \approx 1$. Moreover, kinetic energy is not transformed into heat with perfect efficiency (i.e., $e < 1$) and the target is not pure ice, which reduces even more impact-induced water production. One further problem with this hypothesis is that drainage features appear to be unrelated to secondary impacts (Figure 3d). It is difficult to explain the distribution of secondary craters over a wide area unlike the water source localization in restricted zones (Figure 3a), unless subsurface ice is unevenly distributed. Another hypothesis that might account for the localized ice melting is the directed pressure exerted by the impact itself.

4.3. Water Flow in the Channel

To estimate the flow velocity in the three main channels, the Manning equation was used (e.g., Melosh, 2011):

Table 2
Thermally Eroded Soil According to Equation 11 in Terms of the Ratio Between Melted Soil Thickness to Initial Water Depth for Different Values of the Fraction ϵ of Volume Occupied by Ice, Using $T_0 = 373.15$ K; $T_m = 272.15$ K; $\rho_R = 2{,}700 \frac{kg}{m^3}$

ϵ	0 (rock only)	0.1	0.2	0.3	0.5	1 (pure ice)
$\frac{\Delta D}{D_0}$	1.72	1.58	1.47	1.37	1.20	0.92

Note. Temperature of the Martian soil is taken at −70°C or $T_s = 203.15$ (Carr, 2006).

$$v \approx \frac{1}{n}\left(\frac{g_{\mathrm{MARS}}}{g_{\mathrm{EARTH}}}\right)^{\frac{1}{2}} R_h^{\frac{2}{3}} (\sin\beta)^{\frac{1}{2}} \tag{6}$$

where $n \approx 0.02 - 0.03$ s m$^{-1/3}$ for a smooth and a rough channel, respectively, R_h is the hydraulic radius (i.e., the ratio of the cross-sectional area of the flow to the wetted perimeter or flow boundary i.e. equal to channel depth for very wide channels), and β is the slope angle. The ratio of Mars to Earth gravity fields in Equation 6 is necessary because the Manning coefficient n is calibrated for Earth conditions. Figure 5a illustrates the elevation along the main channel (track in Figure 5b). The characteristic slope angles are shown in Figure 5c. It is observed that the slopes of the main channel are quite gentle, approximately 0.007°, close to the ejecta. However, the terrain exhibits a long system of E-W oriented fracture lines (Figures 5d and 5e). Corresponding to the axis of the fracture system, the terrain has subsided (see MOLA elevation in Figure 5d). Consequently, the main flow has deviated from east to south, following the steeper gradient, resulting in a slope increase by one order of magnitude.

Figure 5e presents the velocities calculated using the slope values compatible with the three channels in the area: the main channel along its west-east direction, and the two secondary channels. Although the observed depth of approximately 15 m corresponds to the maximum degree of soil erosion (Figure 2d), it is unlikely that the maximum discharge reached this level. Thus, several values of water depth, including lower values for the hydraulic radius, are considered in Figure 5e. It follows that the velocities in the main channel were about one to a few meters per second, similar to the velocity of a relatively small river on Earth in alluvial areas. The south-facing secondary channels #1 and #2 could have had maximum speeds of up to 4 m per second. The nature of the discharge, whether gradual, involving a thin layer of water, or more substantial and rapid, remains unknown. Consequently, the run-off time, defined as the duration required for a water parcel to travel through the channel from its inception to the termination point, is estimated to be at least $\approx \frac{40 \text{ km}}{1 \frac{\text{m}}{\text{s}}}$, which equates to approximately 10 hours. Based on MOLA data, the amount of material eroded from the main channel is roughly 1.5 km^3. Assuming an ice content of just 20%, this erosion process would have released at least 0.3 km^3 of water from the subsurface, which subsequently flowed into the lake. The erosion rate was significantly increased by the high temperature of the water on the icy soil, which thermally dislodged the granular component within the ice-bearing matrix.

These velocity values also enable us to estimate the flow duration in the main channels using the relation $\tau \approx V/Q$ where $Q \approx vwR_h$ is the flow discharge (m^3/s) in the main channel and V is the total water volume that has passed through a section of the channel of width w. We measured the volume eroded inside the pit at about 13 km^3. If this volume were due to meltwater coming from below the pit area, it would correspond to a volume of about 13 km$^3/\epsilon$ which, with $\epsilon = 0.2$, would give a volume of 75 km^3 of meltwater coming from the pit area. Section 4.4.3 shows in more detail the thermodynamic calculations for the melted ice beneath the warm lake. It follows that the amount of water at 100°C required to melt this ice is, from Table 2, about 50 km^3. This gives us an idea of the volume of water that escaped from the impact area and contributed to the main channel (the volume of water from melting the ice along the channel and evaluated earlier at 0.3 km^3 was thus only a minor contribution).

We derive time scales of approximately $\tau \approx \frac{V}{Q} = \frac{\mathrm{V}}{v\ w\ R} \approx \frac{50 \times 10^9 \text{ m}^3}{1 \frac{\text{m}}{\text{s}} \times 3{,}000 \text{ m} \times 5 \text{ m}} \approx 3 \times 10^6$ s, assuming a channel width of the order of 3,000 m and a 1 m/s speed at a hydraulic radius of 5 m. These approximations allow us to constrain the water flow duration to about a month. The lake's duration may have been longer subject to freezing and evaporation processes. Under our assumption that $R_h \approx 5$m, $v \approx 1 \frac{\text{m}}{\text{s}}$, it follows that $v < \sqrt{gR_h}$ and, therefore, the flow in the channel was hydraulically subcritical (i.e., it occurred slowly and steadily).

Interestingly, the outflow channels emerging from the ejecta of Tooting develop mostly in the SE direction and do not expand radially from the crater itself, as would be expected in a flat region. It is also surprising that the global slope in this broad region is directed north, opposite to the flow from Tooting. As shown in Figure 4e, small-to medium scale regional gradients surrounding Tooting crater indicate the presence of a basin with the crater at its center. Therefore, while water in the SE direction followed the sharp gradient and incised the channel pattern in the northern sector, any fluid resulting from the melting of ice may have remained stagnant without channel

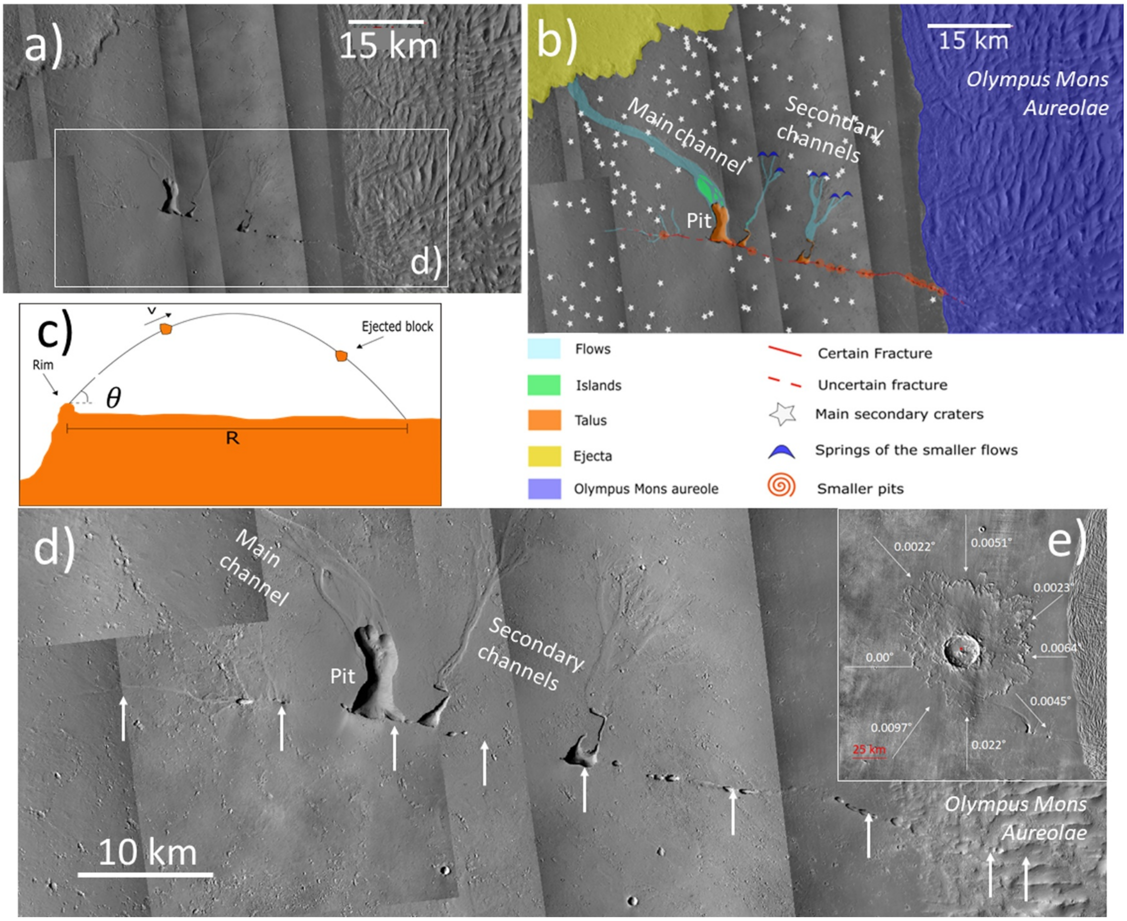

Figure 4. (a) Bare CTX image of the field showing abundant secondary craters from Tooting, and (b) interpreted image showing part of the ejecta, the largest secondary craters (white stars), the erosion channels due to the torrent flows, the islands within the channels, the talus slopes, the syngenetic fractures (faults), the springs of the secondary water flows, and the pits. The legend is shown. (c) illustration for the geometry of a block ejected from the rim at high speed. (d) the long fault crossing Amazonis Planitia is indicated with arrows together with the main channel and the secondary channels (e) Tooting crater and the slopes (in degrees) of the region surrounding it.

incision. Also note that the region west of Tooting is almost perfectly flat and exhibits no outflow discharge, probably due to the impact direction, which released the vast majority of the ejecta to the NE (Wulf et al., 2012).

Finally, although it is difficult to attribute an age to the streambeds using standard crater counting techniques (as the area is small), they are very young, as evidenced by the absence of primary craters, except for those that formed the teardrop-shaped islands and thus predate the event, Figure 3c. Thus, their young age is consistent with the scenario that they have been excavated by the water of the very recent Tooting impact. Note also that the secondary craters have been eroded and modified by subsequent water flow, demonstrating that the channels postdate the secondary craters.

4.4. The Ephemeral Lakes

4.4.1. Formation of the Fractures

The lakes formed at the intersection of water flow with the fracture swarm that crosses the eastern AP at constant latitude (Figures 3–5). We note that fractures are only 80 km from the Tooting crater, which may imply a possible correlation between the two features. The asymmetric distribution of ejecta around the Tooting crater rim (Figure 2) and of the secondary craters (Mouginis-Mark & Boyce, 2012) demonstrates that the impact was not symmetric, and the ejecta spreading area indicates a meteoroid traveling from SW to NE (Figure 2a; Wulf et al., 2012). The fault lines crossing the AP area south of Tooting, approximately perpendicular to the asteroid

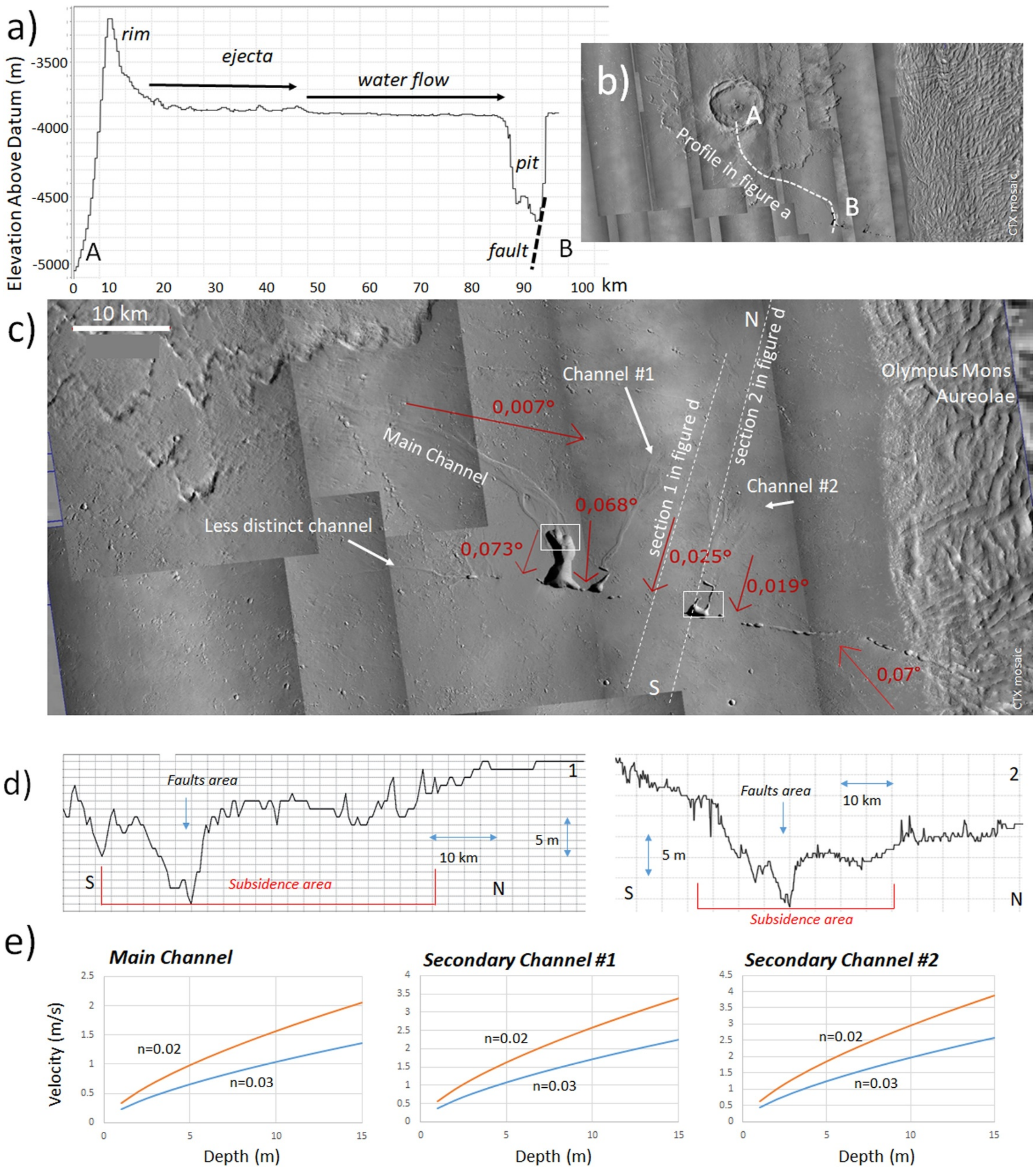

Figure 5. (a) MOLA topographic profile through the main channel following the crater rim through the ejecta, the channel, and into the pit. The line profile is shown in panel (b). (c) the main channel from the ejecta, and the two secondary channels 1 and 2. A less distinct channel from the west partly follows the main fault line. The slopes along channels are indicated. (d) rectilinear sections approximately S-N showing the 30-km-long depression in correspondence to the fault line. The section line is shown in panel (c). (e) Velocities calculated for two different values of the Manning constant n (in units $s/m^{1/3}$) as a function of the hydraulic radius for the three channels shown in Figure (c).

trajectory (Figure 4d), tentatively suggest that the faults were generated by the impact, further enhancing the hydrothermal conductivity in the region (Rodriguez et al., 2005). Examination of craters in AP of similar or slightly smaller size (specifically the four largest craters at 207.116 E, 28.615; 203.92 E, 24.257; 212.419 E, 31.111, and 207.271 E, 20.021) reveals no evidence of associated faults. These craters, however, exhibit symmetrical ejecta, suggesting an impact at high angles.

The timing of the momentum transfer from an asteroid of radius R traveling with impact angle ψ with respect to the ground is on the order of $\Delta t \approx \frac{2R}{U \sin\psi}$, so the resulting horizontal force exerted by the impact can be expressed as

$$F_h \approx \frac{M\,U\cos\psi}{\Delta t} \approx \frac{M\,U^2\,\sin(2\psi)}{4\,\mathrm{R}} = \frac{K\,\sin(2\psi)}{2\,\mathrm{R}} \tag{7}$$

Plugging in the numbers, we obtain $F_h \approx \frac{10^{21}-10^{22}}{2,400}\sin(2\psi) = \left(4.2\times10^{17} - 4.2\times10^{18}\right)\sin(2\psi)$, and with impact angle ψ ranging between 5° and 30°, the force magnitude should be reduced by a factor 0.2–0.8,resulting in a total force of between 8.4×10^{16} N and 4×10^{18} N. The tensile strength of basalt, which can reach tens of MPa (e.g., Perras & Diederichs, 2014), can be significantly reduced in a porous medium. Assuming a nominal strength of $\tau_y = 10$ MPa (consistent with a cohesion of the same order, Crosta et al., 2014), the impact may have potentially opened a fault of depth H such that

$$l\int_0^H \left[\tau_y + \rho g\,y\,k_{\mathrm{pass}}\right]dy \approx F_h \tag{8}$$

where y is the coordinate perpendicular to the ground, $l \approx 100$ km its length, ρ is the density ($\rho \approx 3{,}500$ kg/m^3, here assumed to be greater than that of the regolith and $k_{\mathrm{pass}} \approx 3$ is the passive earth pressure coefficient, since the soil is compressed (Middleton & Wilcock, 1994).

This results in a potential depth H of the order

$$H = \frac{\tau_y}{\rho g k_{\mathrm{pass}}}\left[\sqrt{1+\frac{2F_h\rho g k_{\mathrm{pass}}}{l\;\tau_y^2}} - 1\right] \approx 20\text{ km} \tag{9}$$

The calculation does not account for the target mass and for changes in properties with depth (particularly the tensile strength of rocks, Middleton & Wilcock, 1994), resulting in an unrealistically depth for the fault system. However, the result shows that considerable force was developed at the time of impact, and a deep fault may have been created. Therefore, it is suggested that both the main fault, and the accompanying swarm of secondary faults may have been generated by the impact that created Tooting crater.

As consequence of the impact, regions of Amazonis Planitia north of the fault line experienced a temporary stress of $\sigma \approx \frac{F_h}{LH}$ Which, according to previous estimates, may have reached peak values of approximately $\approx \frac{\left(6\times10^{14} - 2\times10^{16}\ N\right)}{5\times10^{6}} \approx 100$ MPa $-$ 2 GPa. Considering that ice fluidizes at pressures exceeding 200 MPa when temperatures are above -10°C, this directed stress could have facilitated the melting of ice in the secondary channels (see Section 3.2), especially if the ground was also heated by the work done on the rocks by the oriented stress.

4.4.2. Thermokarst and the Ephemeral Lake

If the erosion of the surface was sufficiently fast, the waterfall edge would have retreated without allowing water to accumulate. Conversely, if the rate of water seepage into the deep fault was slower than the inflow from the stream, temporary lakes could have formed within these cavities. Therefore, it is pertinent to evaluate both the potential for thermokarst erosion and the duration of these lakes, considering heat exchange with the environment and evaporation rates.

To estimate the maximum volume of frozen ground that can be melted by a given quantity of warm water, let us consider a body of water (called a "lake" for simplicity) with an initial depth D_0 and a temperature T_0, higher than the ground temperature T_s, assumed constant with depth and time. Assuming minimal heat dissipation to the atmosphere and denoting the lake surface as S, the total thermal energy contained in the lake can be expressed as

$$Q_{\mathrm{water}} = \rho_W C_W (T_0 - T_m)\,SD_0 \tag{10}$$

where T_m is the melting temperature of ice and C_w is the specific heat of water. This energy should be equated to the one absorbed by the bulk ground, and given by

$$Q_{\text{soil}} = \left[\left(\rho_I C_I \epsilon + \rho_R C_R (1-\epsilon)\right)(T_m - T_s) + \rho_I \epsilon \lambda\right] S\,\Delta D \tag{11}$$

where ΔD represents the depth of melted soil, and ϵ is the volumetric fraction of ice, with $1-\epsilon$ being the fraction of rock grains. Table I collects the physical parameters for ice and rock and their numerical values. Regarding porosity values (ϵ), Wilson et al. (2018) suggest a surface hydrogen concentration of around 11% (not all of which may represent water), while the surface porosity of the regolith could be as high as 50% (Clifford & Hillel, 1983). Therefore, the voids within the regolith may not be entirely filled with ice. By equating the two heat contents, that is, setting $Q_{\text{water}} = Q_{\text{soil}}$, and assuming negligible lateral heat loss, we can solve for the depth of soil affected by the thermal exchange

$$\frac{\Delta D}{D_0} = \frac{\rho_W C_W (T_0 - T_m)}{\left(\rho_I C_I \epsilon + \rho_R C_R (1-\epsilon)\right)(T_m - T_s) + \rho_I \epsilon \lambda} \tag{12}$$

Table 2 lists the results for $\frac{\Delta D}{D_0}$ for different pore volume fractions. For an ice fraction of 0.2–0.3, the thermally eroded thickness may be up to 50% higher than the water depth. The melting of ice within the lake contributes additional water that is colder than the existing lake water. However, this cooling effect on the overall water temperature was not included in our simplified estimates.

The evaporation rate of water from both the temporary river and the lake can be estimated using experimental measurements and theoretical calculations. Sears and Moore (2005) examined liquid water just above freezing under Martian conditions with CO_2 partial pressure of 7 mbar and found evaporation rates E on the order of 1 mm/hr. Correcting for Mars' lower gravity reduces this rate to approximately 0.73 mm/hr. These values are consistent with theoretical estimates provided by Ingersoll (1970), within the precision required for this analysis. It is noted that evaporation rates increase exponentially at higher temperatures but are significantly lower for briny water compared to pure water (Sears & Chittenden, 2005). Given uncertainties, including the water composition, we can assume evaporation rates for water in the liquid state just above 0°C to be a fraction of a millimeter per hour to several millimeters per hour, equal to roughly 10–50 m annually. Comparatively, Houston (2006) documented average evaporation rates from terrestrial lakes in the Atacama Desert, with temperature identified as the primary influencing factor. The relationship is described as

$$E\left(\frac{mm}{a}\right) \approx 84.5\,(T_{\text{ave}} - 273.15) + 557 \tag{13}$$

where T_{ave} is the average annual temperature. Typical evaporation rates in the Atacama Desert range from half a meter to three m per year. The lower rates compared to Martian estimates can be attributed to the higher atmospheric pressures on Earth. Kreslavsky and Head (2002) proposed evaporation rates of 3–9 mm per day on Mars for lower temperatures (+10°C) with water in the liquid state, consistent with other findings. In summary, these data suggest that water flowing in channels would suffer minimal evaporative loss during its hours-long flow to the temporary lake, while a lake several hundred-meters could dry out within years or decades if the water remained liquid.

The heat lost by evaporation leads to a reduction in the temperature of the upper water layers of the ephemeral lake. When averaged over the whole water volume, the temperature decrease rate is

$$\frac{dT}{dt} \approx E\frac{\lambda_{\text{evap}}}{C_w D} \tag{14}$$

where λ_{evap} is the latent heat of evaporation (see Table 1), and D is the lake depth.

These estimates indicate rapid evaporation if the water temperature remains constant. However, in the absence of significant water circulation, even warm water will rapidly freeze at the lake surface (Rathbun & Squyres, 2002).

Once the upper layers reach 0°C, the time required for an ice layer of thickness δz to form is approximately (Ashton, 1986)

$$\tau_{\text{ice}} \approx \left[\delta z^2 + 2\delta z \frac{\chi}{H_{\text{ice}}}\right] \frac{\lambda_{\text{evap}}\,\rho_I}{2\chi\Delta T} \tag{15}$$

where $H_{\text{ice}} \approx 10 - 30 \frac{W}{m\,K}$ is the bulk transfer coefficient accounting for the higher temperature of ice with respect to the surrounding environment, χ is the thermal conductivity, and ΔT is the temperature difference between water at the bottom of the ice layer and the external environment. Equation 15 yields an ice thickness growth rate on the order of 1 m annually, consistent with ice growth models in the Arctic (Maykut, 1986; Wadhams, 2014). The presence of an ice layer may contribute to maintaining the heat within the lake. This is not only because sublimation is a slower process than evaporation, as noted by Sears and Moore (2005), but also due to the ability of ice to capture a veneer of windblown dust. This dust layer can significantly reduce the sublimation rate compared with that of clean ice (Chevrier et al., 2007; Douglas & Mellon, 2019; Grimm et al., 2014). According to Chevrier et al. (2007), sublimation rates between 255 and 275 K range between 0.1 and 0.4 mm/hr when a veneer of Mars-1 Martian soil simulant, with thickness ranging from 5 to 200 mm, is spread over the icy surface. The duration of ice loss approximately doubles by doubling the thickness of regolith, but it becomes significantly longer for much thicker layers (Chevrier et al., 2007; Sears & Moore, 2005). Ice blocks in Valles Marineris covered by a thick layer of regolith may last across a very long time (De Blasio & Crosta, 2017). In essence, the sublimation rate of the lake ice cap could vary from months to years, or even longer, depending on the thickness of the windblown regolith layer deposited onto the ice. It can be speculated that as the lacustrine surface dropped below the elevation of the surrounding terrain, it more easily captured windblown particles, thereby reducing the sublimation rate.

5. Present Aspect of the Pits and Slope Streaks

The pits are partially filled with debris falling from the knickpoint and the eroded sides (Figures 3c and 6a). The images show that water has incised the sections, exposing the stratified ground. At least three distinct units can be recognized. In the uppermost part of the wall, HiRISE images reveal a sequence of horizontal layers several tens of meters thick (Figure 7a). These layers consist of cemented blocks of varying size, with the largest reaching a diameter of approximately 10 m. Below these layers, the fallen blocks have formed a talus at the pit margins. The largest boulders are found in the central and deepest parts of the pits, showing a distribution pattern similar to talus slopes on Earth (De Blasio & Sæter, 2009; Turner & Schuster, 1996).

Numerous Slope Streaks can be observed in the three Tooting flow pits (a general discussion over slope streaks morphologies is provided in Appendix A). Specifically, HiRISE images reveal a multitude of streaks above the talus slopes inside the pits (Figure 6). These streaks appear as elongated features, several hundred meters long, and about 30–100 m wide, often branched and shallow. Most lines start from the highest and steepest area of the talus. In principle, this would be consistent with dry flows, which are more unstable on steeper slopes. However, if this was the only case, the starting point would be determined by the local slope angle. Given that the inclination of talus slopes is approximately constant at their tops (Chandler, 1973; Pérez, 1998), there exists an extensive zone below the apex where the gradient remains uniform. Closer inspection reveals that all slope streaks begin precisely at the base of the headwall. Instances of streaks that appear to start mid-slope, such as the ones in Figure 6b marked by a "gap," are typically incomplete and exhibit a whitish hue, indicative of advanced age, significant weathering, and the gradual obliteration of these elusive patterns. Of particular relevance is the dark outline of many slope streaks, which proliferate into multiple, narrow and digitate flows (Figure 7a). Some of these secondary flows follow the headwall contour and terminate after 10–20 m, whereas the main flowline persists for a few hundred meters. Figure 7b delineates the distinction between "main channel" and "secondary channels". As indicated by the arrows in Figure 7a, smaller slope streaks stem from the basal layers of the headwall, while others appear higher in the upper strata. These features indicate that slope streaks may be indicative of moist flows originating from the interface between two strata, with the uppermost layer composed of larger clasts or blocks (Figure 7c). Figure 8 shows a comparison between one of the best-preserved slope streaks within the western pit and water pathways originating from what is postulated as a terrestrial analog.

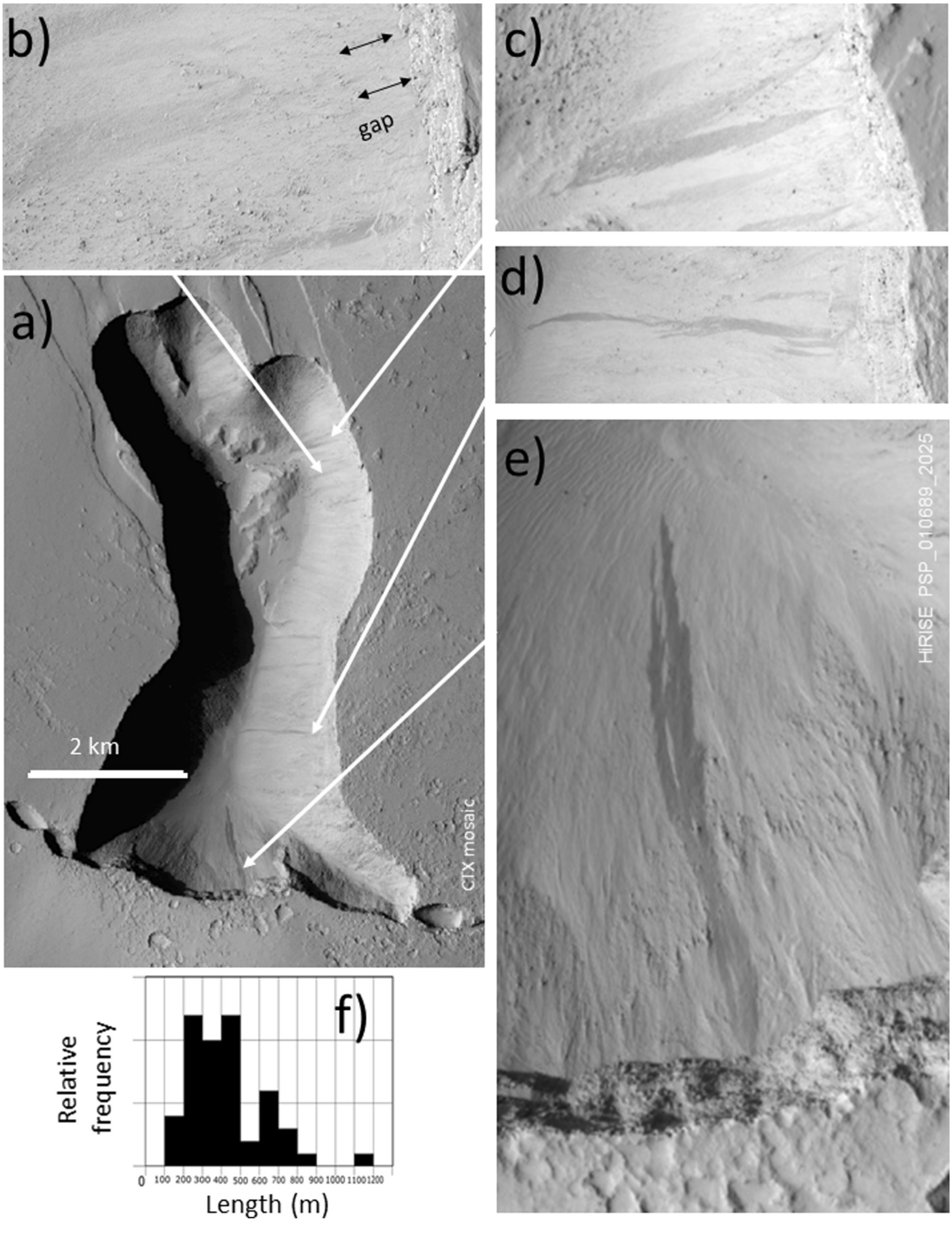

Figure 6. Slope streaks inside the western pit. (a) Image CTX P05_003147_2025_XI_22N151W. (b–e) HiRISE images of the selected areas showing the slope streaks in detail. (f) relative frequency of the lineae observed in the western pit as a function of their length. Note the largest of the slope streaks in the central part of the image springing out precisely at the headwall.

Estimating the typical distance a water flow would travel along a talus slope as it infiltrates through the granular medium is insightful. Our calculations, detailed in Appendix B, assume a talus hydraulic conductivity between 0.001 m/s and 0.1 m/s (i.e., between coarse sand and gravel), a slope of $\beta = 36°$, and an initial depth of the water source above ground level of $h_0 = 1$ m. We find a length $L \approx 160$ m for gravel, $L \approx 1.6$ km for very coarse sand,

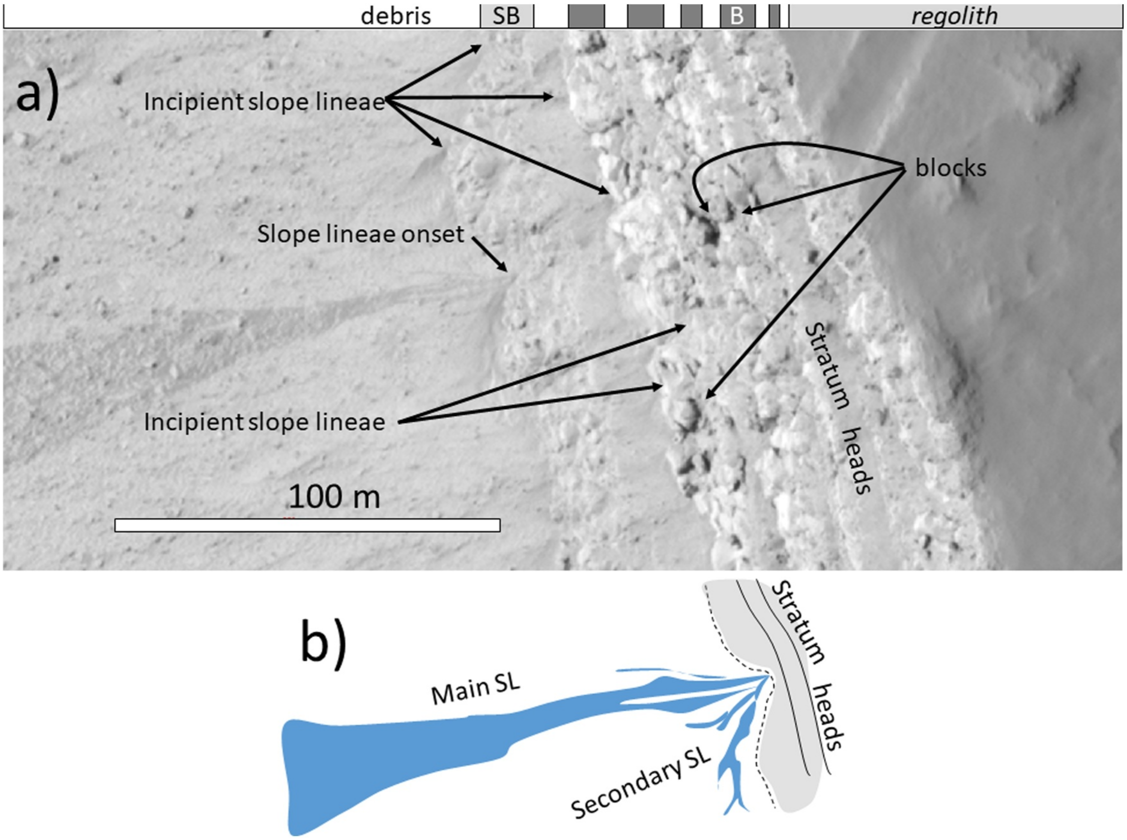

Figure 7. (a) One example of slope streaks from the headwall. Note that in addition to the main slope streaks, there are also incipient lineae from the points indicated with arrows. The main slope line (as also shown in the sketch in b) branches at the headwall through numerous secondary channels, probably following the local slope and running partly parallel to the headwall. The origination of the slope streaks is seen especially from the lowermost layer but also partly from some upper layers. HiRISE image PSP 010689 2025.

and $L \approx 16$ km for coarse sand. The latter value is consistent with observations, suggesting a predominance of mostly coarse sand on the talus. Reducing the water source height from one m to 10 cm reduces the water runout by less than 10%, making it also compatible with fine sand (permeability of 10^{-5} m/s), which can be reasonable for wind-blown particles. Despite uncertainties, these estimates indicate water as a plausible explanation for SL in these pits.

We suggest that the slope streaks in the Amazonis Planitia pits result from ice melting in intermediate layers. Present levels of insolation are inadequate for surface ice melting on Mars (Ojha et al., 2015), but insolation may have contributed to the melting of brines and subsurface ice (Clow, 1987). We suggest that an important contribution to the melting and re-generation of the frozen aquifer occurred when warm water filled the lake and heat diffused to the surface at times of the order of $\delta_m \approx 55\sqrt{\tau_c}$ as per Equation 1. The heat wave from the warm water in the lake could have reached approximately 50–60 m within the surrounding terrain during the lake lifetime. The one-dimensional heat equation with boundary conditions $T = T_S(t)$at $x = 0$ (lake temperature decaying in time) is

$$T(x,t) = \int_0^t \frac{x\,T_L(t')}{\sqrt{4\pi \frac{\chi}{\rho C}(t-t')^3}} \exp\left(-\frac{x^2}{4\frac{\chi}{\rho C}(t-t')}\right) dt' \tag{16}$$

and a solution to this equation is shown in Figure 9c. Note that, as the lake depth decreases due to evaporation and it cools (Figure 9d) the heat wave propagates for longer distances and remains active for several decades. We hypothesize that heat from the top of the reservoir reached the caprock zone, melting the underground ice and

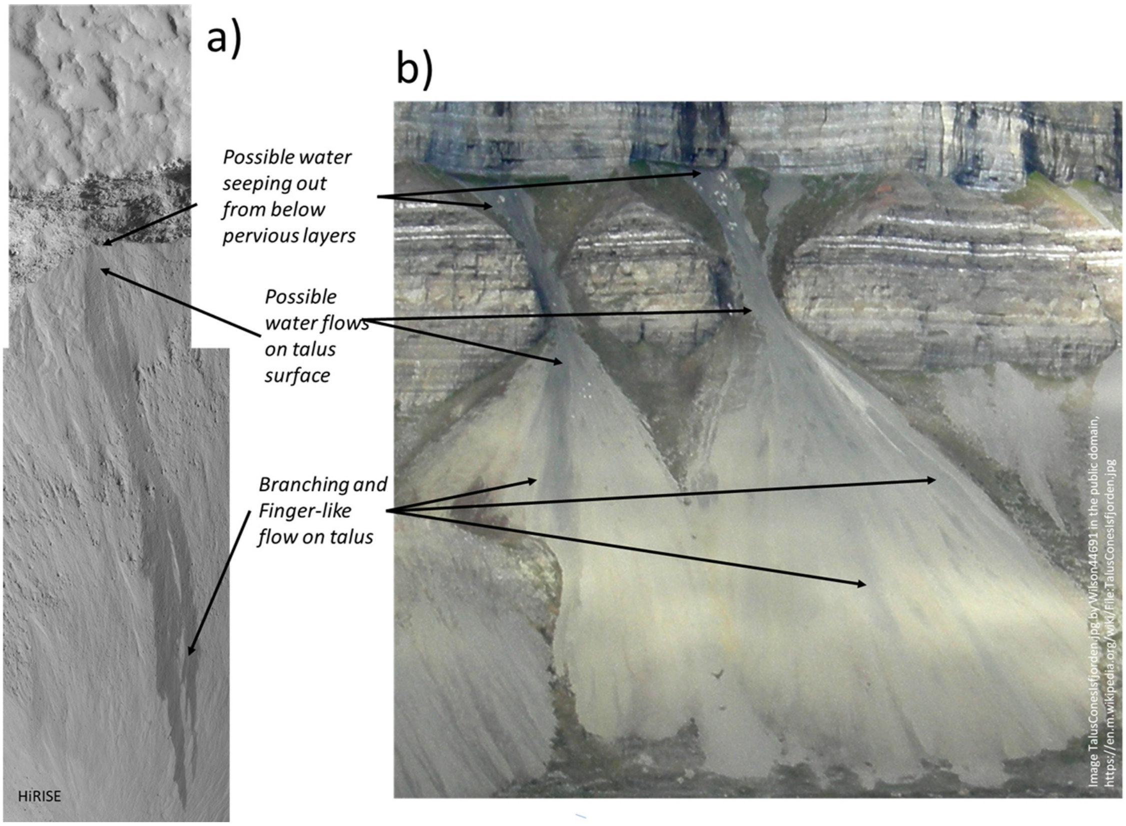

Figure 8. Comparison between one slope linea (a) (the same as of Figure 6e) and (b) water flows from the boundary between pervious and impervious layers in an example from Isfjord in Svalbard. Selected part of a larger image by professor Mark A. Wilson of public domain.

helping to create a temporary aquifer from which the slope streaks could have developed. This process, like all water-related processes on Mars, could have been facilitated by dissolved salts that lower the freezing point (Ojha et al., 2015). Furthermore, this does not rule out solar radiation which, concurrently with the heat wave, contributed reaching the melting point of the brine (striations on the slopes are also observed in isolated areas not affected by the warm water, such as in the Tooting area). Therefore, streaks in the pits may indicate the existence of a potential aquifer within the cryosphere, ready to temporarily melt and discharge when thermally perturbed. The cryosphere ice does not need to exceed 0°C to melt, as salts in the ice decrease the activity of the solution (e.g., Chevrier & Rivera-Valentin, 2012; Mitchell & Christensen, 2016). Figure 9a summarizes this concept in a schematic cross-section of one of the pits. Our interpretation is consistent with the model by Abotalib and Heggy (2019), who found that structural disturbances in briny aquifers could generate numerous slope streaks from the head of fault lines. A difference from Abotalib and Heggy's (2019) findings is that the aquifers they examined were deeper, up to 400–600 m, with water ascending through highly conductive fault lines. We also point out that the tracks of slope streaks may appear "fresh" but be old in temporal perspective, as demonstrated by the commonness of lineae on thermally undisturbed surfaces such as the Olympus Mons aureoles, which may be relatively old.

6. Reconstructing the Hydrogeological History of the Area

Figure 10 provides a chronological representation of the events that led to the formation of ground ice in Amazonis Planitia during the Hesperian-Amazonian era, followed by the late hydrological cycle induced by the Tooting impact. During the transition from the Hesperian to the Amazonian, oceanic waters filled the Amazonis Planitia basin (panel 1 of Figure 10). Panel 2 illustrates the western aureole of Olympus Mons descending onto this oceanic terrain, possibly when water was still present (De Blasio, 2011). With the decline in atmospheric pressure, liquid water vanished from the Mars surface. Some of the water froze to ice, permeating the Martian surface layers, protected from sublimation into the atmosphere by the insulating properties of the porous soil. This

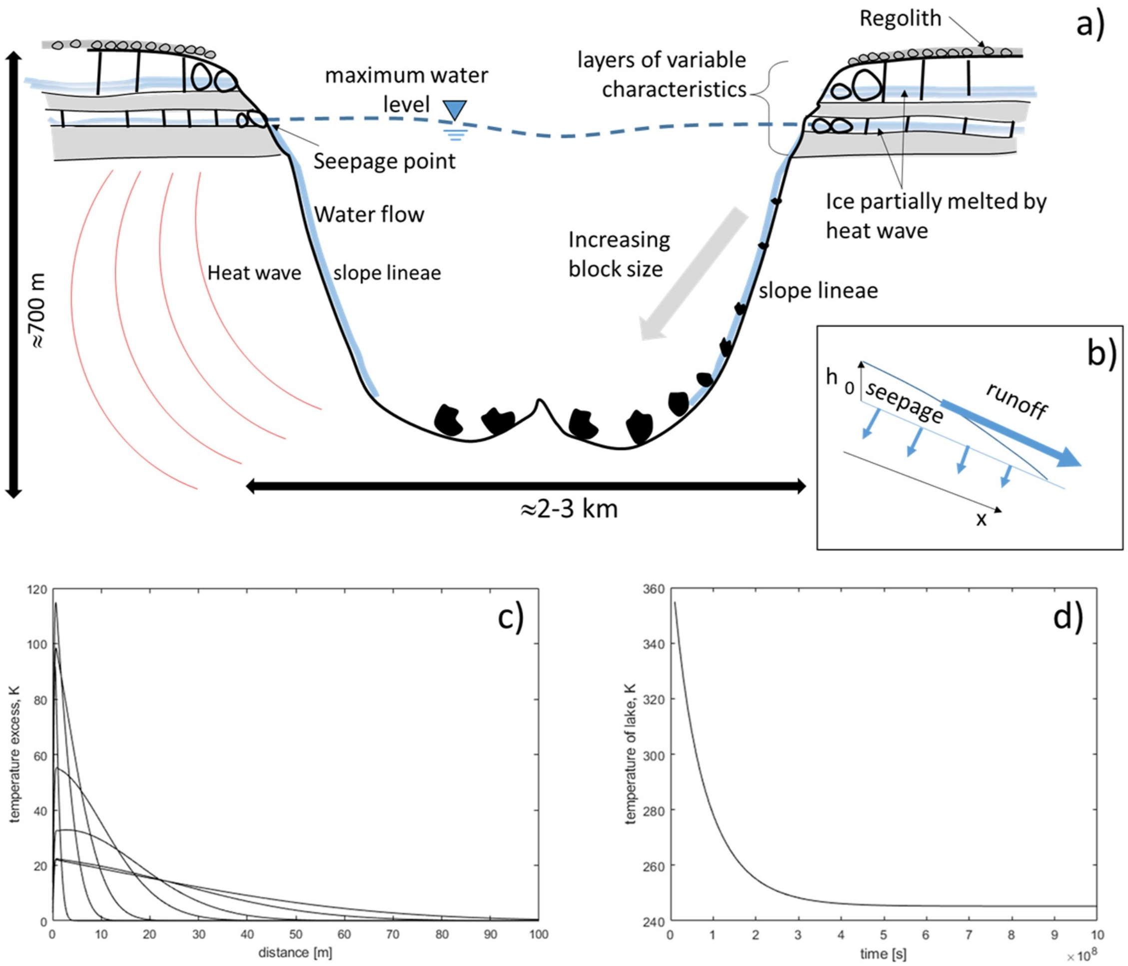

Figure 9. (a) Highly schematic view of the stratigraphic relationship between the strata, talus, and the aquifer of the large pit, along an ideal section from west to east. (b) Scheme for the calculation of the maximum runout of a slope line, interpreted as a superficial water flow (Appendix A). (c) The excess temperature with respect to the soil temperature of 245 K due to a lake with water initially at 373.15 K and level 700 m along the distance for different times calculated with Equation 16 (d) The temperature of the water lake calculated with the equations shown in the supplemental material.

ice persisted for 3 billion years (panel 3). More recently (about 3 million years age), the oblique impact that created the Tooting crater occurred (panel 4), likely creating the extensive EW-trending fault that traverses Amazonis Planitia. The impact melted nearby ice, releasing water that flowed downstream. We base this inference on the idea that Tooting was a very recent event (certainly the most recent dramatic event within a radius of about 300 km around the study area) and that the regional morphology and slope angles were not significantly modified in the time since the Tooting impact. Simultaneously, the ejected debris was hurled over great distances, likely thawing the ground and thus contributing to the hydrological cycle. Southward-flowing water was intercepted by the fault line, where it cascaded, carving out waterfalls and caverns and forming temporary lakes, creating three large pits and some smaller ones (panels 6 and 7). The water disappeared in a geologically short period (6). Heat from the lakes also diffused laterally to the edges of the pits, melting a fraction of the briny ice and creating a temporary aquifer. The remains of these pits are now partially filled with talus debris, resulting from the weathering of the upper layers and downward movement of blocks. Numerous slope streaks have formed on top of the talus, interpreted here as water flows originating from the upper wall of the layers. These slope streaks represent the most recent geological features within the pits.

7. Conclusions

The Tooting impact event on Mars was used as a natural laboratory for understanding planetary hydrological phenomena due to the catastrophic release of water. The presence of abundant ground ice in the area, considered

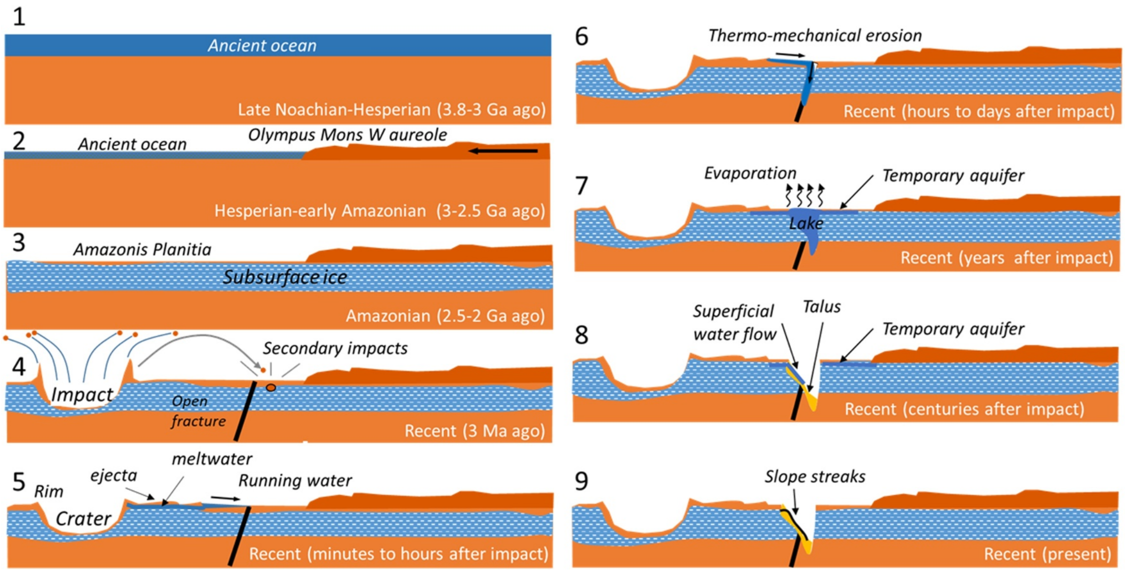

Figure 10. Scheme showing the hydrological history of the area as resulting from the present study. See text for explanation. The first and second panels embrace the scenario of the ancient Oceanus Borealis; as an alternative, the subsequent ice from panel 3 was due to flooding rather than an ocean.

by some researchers to be the bottom of the giant "Oceanus Borealis," or by others to be the bed of water-flooded lava plains, significantly influenced the ensuing events. The morphological features observed in Amazonis Planitia not only attest to the dynamic response of the Martian terrain to asteroid impacts but also highlight the complex interplay between thermal energy and icy substrates. Our findings reveal that the hot water, generated by the impact-induced thermal release, carved deep erosional landforms into the icy ground despite the rapidity of the hydrological events from a geological perspective. The discovery of fault-induced ephemeral lakes, lodged inside pits created by ice melting and waterfall erosion, suggests a novel mechanism for the formation and longevity of ephemeral water bodies on Mars, influenced by both atmospheric conditions and subsurface ice dynamics. Their duration varied from several months to years, depending on the rate of sublimation from the frozen, regolith-bearing lake surface and on the water levels in the lakes. Within the pits, slope streaks are currently observed, morphologically consistent with water flows from a surface icy layer transformed into a temporary aquifer by the heat released from the ephemeral lakes.

This work highlights the importance of considering both immediate and long-term geological processes in shaping planetary surfaces. A key conclusion of this work is the significant role played by groundwater and shallow ice in Amazonis Planitia, and the hydrological cycles that may have occurred in Mars's past. The evolution of such "warm" river networks and the amount of water involved can improve our understanding of impact mechanics, delineate the amount of ice embedded in the soil, and shed light on the dynamics that shaped these distinctive river networks on Mars.

Appendix A: Slope Streaks and Slope Lineae

Slope streaks (SSs) are widespread linear features on Martian slopes, manifesting as dark streaks hundreds of meters in length and tens of meters in width against a lighter background (Carr, 2006; McEwen et al., 2011). These features are found on Martian slopes and much less frequently on rocky outcrops. The significance of SS as potential indicators of liquid water activity and their astrobiological implications for Mars are well recognized (e.g., Carr, 2006). Similar to slope streaks are slope lineae (SL) which are shorter and develop at steeper gradients (Stillman et al., 2024). The distinction between the two is not always apparent, and the two denominations have been frequently used invariably. Time-lapse imaging of the same location has revealed that certain SLs, known as "Recurring Slope streaks" (RSL), exhibit periodic activity, intensifying in summer and nearer the equator (McEwen et al., 2011). RSLs are potentially linked to contemporary groundwater seepage from recent gullies at mid-to high latitudes, possessing high erosive potential (Malin & Edgett, 2000).

Invariably directed downwards and along trajectories typically exceeding 30°, SSs and SLs are unquestionably governed by gravitational forces, yet the precise nature of the flowing material remains elusive and subject to speculation (Dundas et al., 2017). Some researchers hypothesize that the low albedo is the result of water-rich flows originating from outcrops surrounding the talus slopes (e.g., Levy, 2012; Stillmann et al., 2014). Alternatively, these mass flows could represent minor dry avalanches capable of removing the superficial weathered regolith layer, thus exposing the darker substrate. Other transient explanations invoke small landslides and avalanches, somewhat cohesive debris flows (suggesting water involvement, e.g., Mellon & Phillips, 2001), or briny water as the trigger for lineae (McEwen et al., 2014). The recurrent nature of RSLs would necessitate a rapid supply of water, implying the presence of an aquifer within the rock masses. However, recent studies have shown that RSLs are inclined at an almost constant angle, consistent with the regolith's angle of repose, indicating a predominantly dry deposition (Dundas et al., 2017). The lack of HiRISE images depicting the study area over a specific time makes it difficult to assess the periodicity of such features in the case under study.

Dry flows over sand dunes on the leeward side of desert barchans typically form an hourglass-shaped profile with a pronounced incision in the area of instability and a relatively thick swell (Barale, 2015; Breton et al., 2008), a geometry that is replicated in laboratory experiments with artificial dry flows (Sutton et al., 2013). Martian dry flows bear resemblance to their terrestrial analogs and differ from the rectilinear shape characteristic of SSs and SLs (Cornwall et al., 2018). Furthermore, even shallow flows tend to cover a broad area, leading to the expectation of accumulated sand at the front of the flows. However, imagery does not support this occurrence. Dundas (2020) suggested that some newly formed streaks that consistently form on Martian slopes might be dry flows, and Dundas et al. (2017) observed that most lineae initiate on slopes between 28° and 38°, regardless of their length. Since these angles are comparable with the angles of repose for most granular materials, and because dry surface avalanches tend to occur around these angles (e.g., Middleton & Wilcock, 1994), Dundas et al. (2017) concluded that lineae are likely related to dry avalanches. Nonetheless, the initial slope angle also fits a "wet" interpretation of the slope of the lineae, as most of the SSs and SLs, including those studied here, start just below the cap rock in the uppermost talus zone, where talus slopes typically acquire the angle of repose (Peres, 1998), but Stillman et al. (2024) prefer the "dry" flow model for the slope streaks within the Olympus Mons aureolae.

Appendix B: Estimating the Length of Reach of Water Runoff Along a Permeable Slope

We assume that at the base of the headwall rocky layers, water flows with a height h_0 (Figure 9b). In the absence of absorption by the soil, this height h would vary along the talus following the standard equation of steady-state hydraulics (e.g., Todd & Mays, 2004)

$$\frac{dh}{dx} = s\,\frac{h^3 - h_c^3\left(\frac{C_D}{s}\right)}{h^3 - h_c^3} \tag{B1}$$

where x is the horizontal coordinate, $h_c^3 = \frac{q^2}{w^2 g_{\mathrm{MARS}}}$ is the critical height, q is the discharge (in cubic meters per second), w is the width (m), $s = \tan\beta$ is the slope, g_{MARS} is Mars gravity field $\left(\frac{\mathrm{m}}{\mathrm{s}^2}\right)$ (here re-defined to distinguish it from the Earth field g_{EARTH}), and C_D is the friction coefficient against the bed, related to Manning's coefficient n as $C_D = n^2 h^{-1/3} g$. If water percolates into the soil, the thickness of the water layer traveling along the talus slope will change as a function of the distance along the slope with an additional term like

$$\frac{dh}{dx} = \frac{dh}{dt}\frac{dt}{dx} + s\,\frac{h^3 - h_c^3\left(\frac{C_D}{s}\right)}{h^3 - h_c^3} = -\frac{K}{U} + s\,\frac{h^3 - h_c^3\left(\frac{C_D}{s}\right)}{h^3 - h_c^3} \tag{B2}$$

where K is the hydraulic conductivity (in m/s) and the velocity of the runoff water flow is estimated using Manning's formula

$$U \approx \frac{1}{n}\left(\frac{g_{\mathrm{MARS}}}{g_{\mathrm{EARTH}}}\right)^{\frac{1}{2}} \mathrm{h}^{\frac{2}{3}}\, \mathrm{s}^{1/2} \tag{B3}$$

An estimate for the critical height when the Froude number equals one is

$$h_c^3 = \frac{h_0^2 U^2}{g_{\mathrm{MARS}}} \approx 30 - 40 \text{ m}^3 \,. \tag{B4}$$

$$\text{Moreover, } \frac{C_D}{s} = \frac{n^2 g_M}{h^{\frac{1}{3}} s} \approx 0.006 \ll 1.$$

These two estimates allow us to simplify Equation B2 as

$$\frac{dh}{dx} = -\frac{K}{U} - s\frac{h^3}{h_c^3} = -\frac{Kn}{\left(\frac{g_{\mathrm{MARS}}}{g_{\mathrm{EARTH}}}\right)^{\frac{1}{2}} h^{\frac{2}{3}} s^{\frac{1}{2}}} - s\frac{h^3}{h_c^3} \tag{B5}$$

Using (Equations B3 and B4) and integrating from the initial position $x = 0$ where the thickness of the water layer is h_0 and h, after some algebra the solution to the differential equation is

$$h(x) = \left[h_0^{\frac{1}{3}} e^{-\frac{\gamma x}{3}} - \frac{\alpha}{\gamma}\left(1 - e^{-\frac{\gamma x}{3}}\right)\right]^{1/3} \tag{B6}$$

where $\alpha = \frac{Kn}{\left(s \frac{g_{\mathrm{MARS}}}{g_{\mathrm{EARTH}}}\right)^{\frac{1}{2}}}$ and $\gamma = n^2 g_E$.

The flow stops along the talus after a length L where $h(L) \approx 0$ which gives

$$L = \frac{3}{\gamma}\ln\left[1 + \frac{\gamma}{\alpha} h_0^{\frac{1}{3}}\right] \tag{B7}$$

Using $n = 0.04 \text{ m}^{-\frac{1}{3}}$ s (rough soil), average $\beta = 30°$, $h_0 = 1$ m, it follows from Equation B7 that $L \approx 1{,}905$; 1,465; 1,025; 594; 218 m with hydraulic conductivities chosen as.

$K = 10^{-5}\frac{\text{m}}{\text{s}}$; $10^{-4}\frac{\text{m}}{\text{s}}$; $10^{-3}\frac{\text{m}}{\text{s}}$; $10^{-2}\frac{\text{m}}{\text{s}}$; $10^{-1}\frac{\text{m}}{\text{s}}$ (values ranging between silt to fine gravel). The last two data, relating to a soil composed of particles ranging in size from sand and gravel, are those that best fit the length, as shown in Figure 6g. Evidently, although the crudeness of the model and especially the poorly constrained values of the height h_0 and of the permeability prevent a precise evaluation, the results are encouraging in interpreting the slope streaks in the Tooting pits as the result of water flow on a permeable soil.

Conflict of Interest

The authors declare no conflicts of interest relevant to this study.

Data Availability Statement

The Mars data used for investigating the topography and the optical and infrared images are available from the NASA Data System (Christensen et al., 2004; Malin et al., 2007; Smith et al., 2001), and ESA (Neukum & Jaumann, 2004).

Acknowledgments
We acknowledge the financial support by the project "ATEQC—Progetti di ricerca Ateneo-quota competitiva; Univ. Milano Bicocca". Open access publishing facilitated by Universita degli Studi di Milano-Bicocca, as part of the Wiley - CRUI-CARE agreement.

References

Abotalib, A. Z., & Heggy, E. (2019). A deep groundwater origin for recurring slope streaks on Mars. *Nature Geoscience*, *12*(4), 235–241. https://doi.org/10.1038/s41561-019-0327-5
Abramov, O., & Kring, D. A. (2005). Impact-induced hydrothermal activity on early Mars. *Journal of Geophysical Research*, *110*(E12). https://doi.org/10.1029/2005JE002453
Ashton, G. D. (Ed.) (1986). *River Lake ice engineering*. Water Resources Publications.
Baker, V. R., Hamilton, C. W., Burr, D. M., Gulick, V. C., Komatsu, G., Luo, W., et al. (2015). Fluvial geomorphology on Earth-like planetary surfaces: A review. *Geomorphology*, *245*, 149–182. https://doi.org/10.1016/j.geomorph.2015.05.002
Baker, V. R., Strom, R. G., Gilick, V. C., Kargel, J. S., Komatsu, G., & Kale, V. S. (1991). Ancient oceans, ice sheets and the hydrological cycle on Mars. *Nature*, *352*(6336), 589–594. https://doi.org/10.1038/352589a0

Barale, L. (2015). Footstep-triggered grain flows on the lee side of a desert sand dune (Erg Chebbi, Morocco). *International Journal of Earth Sciences: Geologische Rundschau*, *104*(8), 2213–2214. https://doi.org/10.1007/s00531-015-1246-3

Barlow, N. G. (2005). A review of Martian impact crater ejecta structures and their implications for target properties. In *Large meteorite impacts* (III ed.), (Vol. 384, pp. 433–442). The Geological Society of America.

Barlow, N. G., & Bradley, T. L. (1990). Martian impact craters: Correlations of ejecta and interior morphologies with diameter, latitude, and terrain. *Icarus*, *87*(1), 156–179. https://doi.org/10.1016/0019-1035(90)90026-6

Barlow, N. G., & Perez, C. B. (2003). Martian impact crater ejecta morphologies as indicators of the distribution of subsurface volatiles. *Journal of Geophysical Research*, *108*(E8). https://doi.org/10.1029/2002JE002036

Barr, A. C., & Citron, R. I. (2011). Scaling of melt production in hypervelocity impacts from high-resolution numerical simulations. *Icarus*, *211*(1), 913–916. https://doi.org/10.1016/j.icarus.2010.10.022

Bramson, A. M., Byrne, S., Putzig, N. E., Sutton, S., Plaut, J. J., Brothers, T. C., & Holt, J. W. (2015). Widespread excess ice in Arcadia Planitia, Mars. *Geophysical Research Letters*, *42*(16), 6566–6574. https://doi.org/10.1002/2015GL064844

Breton, C., Lancaster, N., & Nickling, W. G. (2008). Magnitude and frequency of grain flows on a desert sand dune. *Geomorphology*, *95*(3–4), 518–523. https://doi.org/10.1016/j.geomorph.2007.07.004

Campbell, B., Carter, L., Phillips, R., Plaut, J., Putzig, N., Safaeinili, A., et al. (2008). SHARAD radar sounding of the Vastitas Borealis Formation in Amazonis Planitia. *Journal of Geophysical Research*, *113*(E12). https://doi.org/10.1029/2008JE003177

Carr, M. (2006). *The surface of Mars*. Cambridge University Press.

Carr, M. H., & Head III, J. W. (2003). Oceans on Mars: An assessment of the observational evidence and possible fate. *Journal of Geophysical Research*, *108*(E5). https://doi.org/10.1029/2002JE001963

Chandler, R. J. (1973). The inclination of talus, arctic talus terraces, and other slopes composed of granular materials. *The Journal of Geology*, *81*(1), 1–14. https://doi.org/10.1086/627804

Chevrier, V., Sears, D. W., Chittenden, J. D., Roe, L. A., Ulrich, R., Bryson, K., et al. (2007). Sublimation rate of ice under simulated Mars conditions and the effect of layers of mock regolith JSC Mars-1. *Geophysical Research Letters*, *34*(2). https://doi.org/10.1029/2006GL028401

Chevrier, V. F., & Rivera-Valentin, E. G. (2012). Formation of recurring slope streaks by liquid brines on present-day Mars. *Geophysical Research Letters*, *39*, L21202. https://doi.org/10.1029/2012GL054119

Christensen, P. R., Jakosky, B. M., Kieffer, H. H., Malin, M. C., McSween, H. Y., Nealson, K., et al. (2004). The Thermal Emission Imaging System (THEMIS) for the Mars 2001 Odyssey mission. *Space Science Reviews*, *110*(1–2), 85–130. https://doi.org/10.1023/B:SPAC.0000021008.16305.94

Clifford, S. M., & Hillel, D. (1983). The stability of ground ice in the equatorial region of Mars. *Journal of Geophysical Research*, *88*(B3), 2456–2474. https://doi.org/10.1006/icar.2001.6671

Clifford, S. M., & Parker, T. J. (2001). The evolution of the Martian hydrosphere: Implication for the fate of a primordial ocean and the current state of the northern plains. *Icarus*, *154*, 40–79.

Clow, G. D. (1987). Generation of liquid water on Mars through the melting of a dusty snowpack. *Icarus*, *72*(1), 95–127. https://doi.org/10.1016/0019-1035(87)90123-0

Cornwall, C., Bourke, M. C., Jackson, D. W., & Cooper, J. A. G. (2018). Aeolian slipface dynamics and grainflow morphologies on Earth and Mars. *Icarus*, *314*, 311–326. https://doi.org/10.1016/j.icarus.2018.05.033

Costard, F., Aguirre-Puente, J., Greeley, R., & Makhloufi, N. (1999). Martian fluvial-thermal erosion: Laboratory simulation. *Journal of Geophysical Research*, *104*(E6), 14091–14098. https://doi.org/10.1029/1999je900020

Costard, F., & Baker, V. R. (2001). Thermokarst landforms and processes in Ares Vallis, Mars. *Geomorphology*, *37*(3–4), 289–301. https://doi.org/10.1016/s0169-555x(00)00088-x

Costard, F. M., & Kargel, J. S. (1995). Outwash plains and thermokarst on Mars. *Icarus*, *114*(1), 93–112. https://doi.org/10.1006/icar.1995.1046

Crosta, G. B., Utili, S., De Blasio, F. V., & Castellanza, R. (2014). Reassessing rock mass properties and slope instability triggering conditions in Valles Marineris, Mars. *Earth and Planetary Science Letters*, *388*, 329–342. https://doi.org/10.1016/j.epsl.2013.11.053

Dapremont, A. M., & Wray, J. J. (2021). Igneous or mud volcanism on Mars? The case study of Hephaestus Fossae. *Journal of Geophysical Research: Planets*, *126*(2), e2020JE006390. https://doi.org/10.1029/2020je006390

De Blasio, F. V. (2011). The aureole of Olympus Mons (Mars) as the compound deposit of submarine landslides. *Earth and Planetary Science Letters*, *312*(1–2), 126–139. https://doi.org/10.1016/j.epsl.2011.09.019

De Blasio, F. V. (2018). The pristine shape of Olympus Mons on Mars and the subaqueous origin of its aureole deposits. *Icarus*, *302*, 44–61. https://doi.org/10.1016/j.icarus.2017.11.003

De Blasio, F. V., & Crosta, G. B. (2017). Modelling Martian landslides: Dynamics, velocity, and paleoenvironmental implications. *The European Physical Journal Plus*, *132*(11), 1–20. https://doi.org/10.1140/epjp/i2017-11727-x

De Blasio, F. V., Crosta, G. B., Fusetti, D., & Valbuzzi, E. (2024). The glacial and periglacial evolution of Coprates Chasma (Valles Marineris, Mars). *Geomorphology*, *467*, 109444. https://doi.org/10.1016/j.geomorph.2024.109444

De Blasio, F. V., & Sæter, M. B. (2009). Small-scale experimental simulation of talus evolution. *Earth Surface Processes and Landforms*, *34*(12), 1685–1692. https://doi.org/10.1002/esp.1861

Dickeson, Z. I., & Davis, J. M. (2020). Martian oceans. *Astronomy and Geophysics*, *61*(3), 3.11–3.17. https://doi.org/10.1093/astrogeo/ataa038

Douglas, T. A., & Mellon, M. T. (2019). Sublimation of terrestrial permafrost and the implications for ice-loss processes on Mars. *Nature Communications*, *10*(1), 1716. https://doi.org/10.1038/s41467-019-09410-8

Dundas, C. M. (2020). Geomorphological evidence for a dry dust avalanche origin of slope streaks on Mars. *Nature Geoscience*, *13*(7), 473–476. https://doi.org/10.1038/s41561-020-0598-x

Dundas, C. M., Byrne, S., & McEwen, A. S. (2015). Modeling the development of Martian sublimation thermokarst landforms. *Icarus*, *262*, 154–169. https://doi.org/10.1016/j.icarus.2015.07.033

Dundas, C. M., McEwen, A. S., Chojnacki, M., Milazzo, M. P., Byrne, S., McElwaine, J. N., & Urso, A. (2017). Granular flows at recurring slope streaks on Mars indicate a limited role for liquid water. *Nature Geoscience*, *10*(12), 903–907. https://doi.org/10.1038/s41561-017-0012-5

Dundas, C. M., Mellon, M. T., Posiolova, L. V., Miljković, K., Collins, G. S., Tornabene, L. L., et al. (2023). A large new crater exposes the limits of water ice on Mars. *Geophysical Research Letters*, *50*(2), e2022GL100747. https://doi.org/10.1029/2022GL100747

Flynn, G. J., Consolmagno, G. J., Brown, P., & Macke, R. J. (2018). Physical properties of the stone meteorites: Implications for the properties of their parent bodies. *Geochemistry*, *78*(3), 269–298. https://doi.org/10.1016/j.chemer.2017.04.002

French, H. M. (2007). *The periglacial environment, ThirdEdition*. John Wiley and Sons Inc.

Fuller, E. R., & Head III, J. W. (2002). Amazonis Planitia: The role of geologically recent volcanism and sedimentation in the formation of the smoothest plains on Mars. *Journal of Geophysical Research*, *107*(E10), 11-1. https://doi.org/10.1029/2002je001842

Garvin, J. B., Soare, R. J., Hepburn, A. J., Koutnik, M., & Godin, E. (2024). Ice exploration on Mars: Whereto and when? In *Ices in the solar System* (pp. 193–219). Elsevier.

Grimm, R. E., Harrison, K. P., & Stillman, D. E. (2014). Water budgets of Martian recurring slope streaks. *Icarus*, *233*, 316–327. https://doi.org/10.1073/pnas.0706977104

Harrison, T. N., Malin, M. C., Edgett, K. S., Shean, D. E., Kennedy, M. R., Lipkaman, L. J., et al. (2010). Impact-induced overland fluid flow and channelized erosion at Lyot Crater, Mars. *Geophysical Research Letters*, *37*(21). https://doi.org/10.1029/2010gl045074

Head, J. W., III, Hiesinger, H., Ivanov, M. A., Kreslavsky, M. A., Pratt, S., & Thomson, B. J. (1999). Possible ancient oceans on Mars: Evidence from Mars Orbiter Laser Altimeter data. *Science*, *286*(5447), 2134–2137. https://doi.org/10.1126/science.286.5447.2134

Horvath, D. G., & Andrews-Hanna, J. C. (2024). The hydrology of the Jezero crater Paleolake: Implications for the climate and limnology of the lake system from hydrological modeling. *Earth and Planetary Science Letters*, *635*, 118690. https://doi.org/10.1016/j.epsl.2024.118690

Houston, J. (2006). Variability of precipitation in the Atacama Desert: Its causes and hydrological impact. *International Journal of Climatology: A Journal of the Royal Meteorological Society*, *26*(15), 2181–2198. https://doi.org/10.1002/joc.1359

Huggett, R., & Shuttleworth, E. (2022). *Fundamentals of geomorphology*. Routledge.

Ingersoll, A. P. (1970). Mars: Occurrence of liquid water. *Science*, *168*(3934), 972–973. https://doi.org/10.1126/science.168.3934.972

Jankowski, D. G., & Squyres, S. W. (1993). Softened impact craters on Mars: Implications for ground ice and the structure of the Martian Megaregolith. *Icarus*, *106*(2), 365–379. https://doi.org/10.1006/icar.1993.1178

Kreslavsky, M. A., & Head, J. W. (2002). Fate of outflow channel effluents in the northern lowlands of Mars: The Vastitas Borealis Formation as a sublimation residue from frozen ponded bodies of water. *Journal of Geophysical Research*, *107*(E12), 4-1. https://doi.org/10.1029/2001JE001831

Lanagan, P. D., McEwen, A. S., Keszthelyi, L. P., & Thordarson, T. (2001). Rootless cones on Mars indicating the presence of shallow equatorial ground ice in recent times. *Geophysical Research Letters*, *28*(12), 2365–2367. https://doi.org/10.1029/2001GL012932

Levy, J. (2012). Hydrological characteristics of recurrent slope streaks on Mars: Evidence for liquid flow through regolith and comparisons with Antarctic terrestrial analogs. *Icarus*, *219*(1), 1–4. https://doi.org/10.1016/j.icarus.2012.02.016

Lucchitta, B. K., Ferguson, H. M., & Summers, C. (1986). Sedimentary deposits in the northern lowland plains, Mars. *Journal of Geophysical Research*, *91*(B13), E166–E174. https://doi.org/10.1029/JB091iB13p0E166

Malin, M. C., Bell III, J. F., Cantor, B. A., Caplinger, M. A., Calvin, W. M., Clancy, R. T., et al. (2007). Context camera investigation on board the Mars Reconnaissance Orbiter. *Journal of Geophysical Research*, *112*(E5). https://doi.org/10.1029/2006JE002808

Malin, M. C., & Edgett, K. S. (2000). Sedimentary rocks of early Mars. *Science*, *290*(5498), 1927–1937. https://doi.org/10.1126/science.290.5498.1927

Maykut, G. A. (1986). The surface heat and mass balance. In *The geophysics of sea ice* (pp. 395–463). Springer US.

McEwen, A. S., Dundas, C. M., Mattson, S. S., Toigo, A. D., Ojha, L., Wray, J. J., et al. (2014). Recurring slope streaks in equatorial regions of Mars. *Nature Geoscience*, *7*(1), 53–58. https://doi.org/10.1038/ngeo2014

McEwen, A. S., Ojha, L., Dundas, C. M., Mattson, S. S., Byrne, S., Wray, J. J., et al. (2011). Seasonal flows on warm Martian slopes. *Science*, *333*(6043), 740–743. https://doi.org/10.1126/science.1204816

Mellon, M. T., & Phillips, R. J. (2001). Recent gullies on Mars and the source of liquid water. *Journal of Geophysical Research*, *106*(E10), 23165–23179. https://doi.org/10.1029/2000JE001424

Melosh, H. J. (1989). *Impact cratering. A geologic process* (p. 245). Oxford University Press.

Melosh, H. J. (2011). *Planetary surface processes* (Vol. 13, p. 534). Cambridge University Press. https://doi.org/10.1017/cbo9780511977848

Middleton, G. V., & Wilcock, P. R. (1994). *Mechanics in the earth and environmental sciences*. Cambridge University Press.

Mitchell, J. L., & Christensen, P. R. (2016). Recurring slope streaks and chlorides on the surface of Mars. *Journal of Geophysical Research: Planets*, *121*(8), 1411–1428. https://doi.org/10.1002/2016JE005012

Morgenstern, A., Hauber, E., Reiss, D., van Gasselt, S., Grosse, G., & Schirrmeister, L. (2007). Deposition and degradation of a volatile-rich layer in Utopia Planitia and implications for climate history on Mars. *Journal of Geophysical Research*, *112*(E6). https://doi.org/10.1029/2006je002869

Mouginis-Mark, P. J., & Boyce, J. M. (2012). Tooting crater: Geology and geomorphology of the archetype large, fresh, impact crater on Mars. *Geochemistry*, *72*(1), 1–23. https://doi.org/10.1016/j.chemer.2011.12.001

Mouginis-Mark, P. J., & Garbeil, H. (2007). Crater geometry and ejecta thickness of the Martian impact crater Tooting. *Meteoritics & Planetary Sciences*, *42*(9), 1615–1625. https://doi.org/10.1111/j.1945-5100.2007.tb00594.x

Mouginot, J., Pommerol, A., Beck, P., Kofman, W., & Clifford, S. M. (2012). Dielectric map of the Martian northern hemisphere and the nature of plain filling materials. *Geophysical Research Letters*, *39*(2). https://doi.org/10.1029/2011GL050286

Murray, J. B., Balme, M. R., Muller, J. P., Kim, J. R., Morley, J., & Neukum, G. (2006). Preliminary observations on new images of the elysium Frozen Sea deposits from HRSC Mars Express.

Nerozzi, S., Tober, B., Holt, J. W., & Ortiz, M. (2020). *Reconstructing the geologic history of Hebrus Valles and Hephaestus Fossae, Mars with SHARAD* (Vol. 2020, p. P016-0004). AGU Fall Meeting Abstracts.

Neukum, G., & Jaumann, R. (2004). HRSC: The high resolution stereo camera of Mars Express. *In: Mars Express: The scientific payload. Ed. by Andrew Wilson, scientific coordination: Agustin Chicarro. ESA SP-1240*, Noordwijk, Netherlands: ESA Publications Division, (Vol. 1240, 17–35). Retrieved from https://sci.esa.int/s/w0oQQlA

Newsom, H. E. (2010). *Heated lakes on Mars* (pp. 93–110). Elsevier.

Ojha, L., Wilhelm, M. B., Murchie, S. L., McEwen, A. S., Wray, J. J., Hanley, J., et al. (2015). Spectral evidence for hydrated salts in recurring slope streaks on Mars. *Nature Geoscience*, *8*(11), 829–832. https://doi.org/10.1038/ngeo2546

Ostrowski, D., & Bryson, K. (2019). The physical properties of meteorites. *Planetary and Space Science*, *165*, 148–178. https://doi.org/10.1016/j.pss.2018.11.003

Page, D. P. (2007). Recent low-latitude freeze–thaw on Mars. *Icarus*, *189*(1), 83–117. https://doi.org/10.1016/j.icarus.2007.01.005

Parker, T. J. (1994). Martian paleolakes and Oceans (p. 200p). Ph.D., Univ. of So. California.

Parker, T. J., Grant, J. A., & Franklin, B. J. (2010). The northern plains: A Martian oceanic basin. *Lakes on Mars*, 249–273.

Pérez, F. (1998). Talus fabric, clast morphology, and botanical indicators of slope processes on the Chaos Crags (California Cascades), USA. *Géographie Physique et Quaternaire*, *52*(1), 47–68.

Perras, M. A., & Diederichs, M. S. (2014). A review of the tensile strength of rock: Concepts and testing. *Geotechnical & Geological Engineering*, *32*(2), 525–546. https://doi.org/10.1007/s10706-014-9732-0

Pierazzo, E., Vickery, A. M., & Melosh, H. J. (1997). A reevaluation of impact melt production. *Icarus*, *127*(2), 408–423. https://doi.org/10.1006/icar.1997.5713

Rathbun, J. A., & Squyres, S. W. (2002). Hydrothermal systems associated with Martian impact craters. *Icarus*, *157*(2), 362–372. https://doi.org/10.1006/icar.2002.6838

Rodriguez, J. A. P., Bourke, M., Tanaka, K. L., Miyamoto, H., Kargel, J., Baker, V., & Berman, D. C. (2012). Infiltration of Martian outflow channel floodwaters into lowland cavernous systems. *Geophysical Research Letters*, *39*(22). https://doi.org/10.7202/004861ar

Rodríguez, J. A. P., Sasaki, S., Dohm, J. M., Tanaka, K. L., Strom, B., Kargel, J., et al. (2005). Control of impact crater fracture systems on subsurface hydrology, ground subsidence, and collapse, Mars. *Journal of Geophysical Research*, *110*(E6). https://doi.org/10.1029/2004je002365

Schaller, M., von Blanckenburg, F., Hovius, N., & Kubik, P. W. (2001). Large-scale erosion rates from in situ-produced cosmogenic nuclides in European river sediments. *Earth and Planetary Science Letters*, *188*(3–4), 441–458. https://doi.org/10.1016/s0012-821x(01)00320-x

Sears, D. W., & Chittenden, J. D. (2005). On laboratory simulation and the temperature dependence of the evaporation rate of brine on Mars. *Geophysical Research Letters*, *32*(23). https://doi.org/10.1029/2005GL024154

Sears, D. W., & Moore, S. R. (2005). On laboratory simulation and the evaporation rate of water on Mars. *Geophysical Research Letters*, *32*(16). https://doi.org/10.1029/2005gl023443

Senft, L. E., & Stewart, S. T. (2008). Impact crater formation in icy layered terrains on Mars. *Meteoritics & Planetary Sciences*, *43*(12), 1993–2013. https://doi.org/10.1111/j.1945-5100.2008.tb00657.x

Smith, D. E., Zuber, M. T., Frey, H. V., Garvin, J. B., Head, J. W., Muhleman, D. O., et al. (2001). Mars Orbiter Laser Altimeter: Experiment summary after the first year of global mapping of Mars. *Journal of Geophysical Research*, *106*(E10), 23689–23722. https://doi.org/10.1029/2000JE001364

Soare, R. J., Osinski, G. R., & Roehm, C. L. (2008). Thermokarst lakes and ponds on Mars in the very recent (late Amazonian) past. *Earth and Planetary Science Letters*, *272*(1–2), 382–393. https://doi.org/10.1016/j.epsl.2008.05.010

Stillman, D. E., Hoover, R. H., Kaplan, H. H., Michaels, T. I., Fenton, L. K., & Primm, K. M. (2024). Comprehensive observations and geostatistics of slope streaks within the Olympus Mons Aureole. *Icarus*, *415*, 116061. https://doi.org/10.1016/j.icarus.2024.116061

Stillman, D. E., Michaels, T. I., Grimm, R. E., & Harrison, K. P. (2014). New observations of Martian southern mid-latitude Recurring slope streaks (RSL) imply formation by freshwater subsurface flows. *Icarus*, *233*, 328–341. https://doi.org/10.1016/j.icarus.2014.01.017

Sturm, S., Kenkmann, T., & Hergarten, S. (2016). Ejecta thickness and structural rim uplift measurements of Martian impact craters: Implications for the rim formation of complex impact craters. *Journal of Geophysical Research: Planets*, *121*(6), 1026–1053. https://doi.org/10.1002/2015JE004959

Sutton, S. L. F., McKenna Neuman, C., & Nickling, W. (2013). Avalanche grainflow on a simulated Aeolian dune. *Journal of Geophysical Research: Earth Surface*, *118*(3), 1767–1776. https://doi.org/10.1002/jgrf.20130

Todd, D. K., & Mays, L. W. (2004). *Groundwater hydrology*. John Wiley and Sons.

Turner, A. K., & Schuster, R. L. (1996). Colluvium and talus. In *Landslides—Investigaton and Mitigation, special report 247. Transportation Research Board* (pp. 525–549). National Research Council, National Academy Press.

Wadhams, P. (2014). *Ice in the Ocean*. CRC Press.

Wang, C. Y., Manga, M., & Wong, A. (2005). Floods on Mars released from groundwater by impact. *Icarus*, *175*(2), 551–555. https://doi.org/10.1016/j.icarus.2004.12.003

Washburn, A. L. (1980). Permafrost features as evidence of climatic change. *Earth-Science Reviews*, *15*(4), 327–402. https://doi.org/10.1016/0012-8252(80)90114-2

Weiss, D. K., & Head, J. W. (2013). Formation of double-layered ejecta craters on Mars: A glacial substrate model. *Geophysical Research Letters*, *40*(15), 3819–3824. https://doi.org/10.1002/grl.50778

Weiss, D. K., & Head, J. W. (2014). *Ejecta mobility of layered ejecta craters on Mars: Assessing the influence of snow and ice deposits*. Department of Geological Sciences, Brown University. https://doi.org/10.1016/j.icarus.2014.01.038

Weiss, D. K., Head, J. W., Palumbo, A. M., & Cassanelli, J. P. (2017). Extensive amazonian-aged fluvial channels on Mars: Evaluating the role of Lyot crater in their formation. *Geophysical Research Letters*, *44*(11), 5336–5344. https://doi.org/10.1002/2017gl073821

Wilson, J. T., Eke, V. R., Massey, R. J., Elphic, R. C., Feldman, W. C., Maurice, S., & Teodoro, L. F. (2018). Equatorial locations of water on Mars: Improved resolution maps based on Mars Odyssey Neutron Spectrometer data. *Icarus*, *299*, 148–160. https://doi.org/10.1016/j.icarus.2017.07.028

Wulf, G., Poelchau, M. H., & Kenkmann, T. (2012). Structural asymmetry in Martian impact craters as an indicator for an impact trajectory. *Icarus*, *220*(1), 194–204. https://doi.org/10.1016/j.icarus.2012.04.025